

Article

A New Regional Background Atmospheric Station in the Yangtze River Delta Region for Carbon Monoxide: Assessment of Spatiotemporal Characteristics and Regional Significance

Yi Lin ¹ , Shan Li ^{1,2}, Yan Yu ^{3,*}, Meijing Lu ⁴, Bingjiang Chen ^{1,2}, Yuanyuan Chen ¹ , Kunpeng Zang ¹, Shuo Liu ¹, Bing Qi ⁵ and Shuangxi Fang ^{1,6,*}

- ¹ Zhejiang Carbon Neutral Innovation Institute & Zhejiang International Cooperation Base for Science and Technology on Carbon Emission Reduction and Monitoring, Zhejiang University of Technology, Hangzhou 310014, China; linyi@zjut.edu.cn (Y.L.); 2112127171@zjut.edu.cn (S.L.); bjchen@zjut.edu.cn (B.C.); yychen91@zjut.edu.cn (Y.C.); zangkunpeng@zjut.edu.cn (K.Z.); shuoliu241@zjut.edu.cn (S.L.)
- ² College of Environmental, Zhejiang University of Technology, Hangzhou 310014, China
- ³ Zhejiang Institute of Meteorological Sciences, Hangzhou 310052, China
- ⁴ Tonglu Meteorological Bureau, Tonglu 311500, China; llllllmj98@163.com
- ⁵ Hangzhou Meteorological Bureau, Hangzhou 310051, China; bill_129@sina.com
- ⁶ Collaborative Innovation Center on Forecast and Evaluation of Meteorological Disasters (CIC-FEMD), Nanjing University of Information Science & Technology, Nanjing 210044, China
- * Correspondence: yuyan321@126.com (Y.Y.); fangsx@zjut.edu.cn (S.F.)

Abstract: A new meteorological station (DMS) was established at the Morning Glory summit in Zhejiang Province to provide regional background information on atmospheric composition in the Yangtze River Delta (YRD) region, China. This study investigated the first carbon monoxide (CO) records at DMS from September 2020 to January 2022. The annual average concentration of CO was 233.4 ± 3.8 ppb, which exceeded the measurements recorded at the other Asian background sites. The winter CO concentration remained elevated but peaked in March in the early spring due to the combined effect of regional emissions within the YRD and transportation impacts of North China and Southeast Asia sources. The diurnal cycle had a nocturnal peak and a morning valley but with a distinct afternoon climb, as the metropolis in the YRD contributed to a local concentration enhancement. The back trajectory analysis and the Weighted Potential Sources Contribution Function (WPSCF) maps highlighted emissions from Anhui, Jiangxi, Zhejiang, and Jiangsu provinces as significant sources. Due to well-mixed air conditions and fewer anthropogenic influences, DMS records closely aligned with the CO averages derived from the Copernicus Atmospheric Monitoring Service (CAMS) covering the YRD, confirming its representativeness for regional CO levels. This study underscored DMS as a valuable station for monitoring and understanding CO spatiotemporal characteristics in the YRD region.

Keywords: carbon monoxide (CO); background observation; spatiotemporal variations; regional representation



Academic Editor: Antonio Donato

Received: 21 December 2024

Revised: 6 January 2025

Accepted: 15 January 2025

Published: 17 January 2025

Citation: Lin, Y.; Li, S.; Yu, Y.; Lu, M.; Chen, B.; Chen, Y.; Zang, K.; Liu, S.; Qi, B.; Fang, S. A New Regional Background Atmospheric Station in the Yangtze River Delta Region for Carbon Monoxide: Assessment of Spatiotemporal Characteristics and Regional Significance. *Atmosphere* **2025**, *16*, 101. <https://doi.org/10.3390/atmos16010101>

Copyright: © 2025 by the authors. Licensee MDPI, Basel, Switzerland. This article is an open access article distributed under the terms and conditions of the Creative Commons Attribution (CC BY) license (<https://creativecommons.org/licenses/by/4.0/>).

1. Introduction

Carbon monoxide (CO) is one of the trace gases contributing to global warming. It plays an important role in the atmospheric carbon cycle and is considered an indirect greenhouse gas [1,2]. CO diminishes the atmospheric oxidizing capacity by reacting with hydroxyl radical (OH) in the troposphere [3]. This reaction reduces the removal rate of other greenhouse gases, which also react with OH, such as methane (CH₄) [1]. The critical CO sources include fossil fuel combustion, biomass burning, and oxidation of

some atmospheric components. Approximately 45% of atmospheric CO comes from the oxidation of CH₄ and other organic compounds in the atmosphere [4]. Biomass burning contributes 20% to 25% of CO emissions in the atmosphere [5].

The primary methods for measuring atmospheric CO concentrations include ground-based observations, satellite remote sensing, and airborne detection [6–8]. Ground-based background observations play a crucial role in validating the accuracy of the other two measurement techniques. In addition to their role in methodological verification, ground-based observations could provide valuable insights into the intensity of human activity, the impacts of climate change, and the effectiveness of policy interventions. However, most ground-based observations are unavoidably impacted by local sources, and very few stations have the background information for regional or even global scales.

CO has been an essential index of air quality monitoring, primarily focused on urban areas. CO plays a crucial role in supporting international efforts, particularly in relation to the United Nations Sustainable Development Goals (SDGs), especially SDG 13 (Climate Action) and SDG 11 (Sustainable Cities and Communities). Continuous CO monitoring provides the data necessary to track progress toward the SDGs, enabling better policy-making at both the local and global levels. Stakeholders can assess the impact of transitioning from fossil fuels to renewable energy sources with CO observation records. However, the present observation networks often overlook variations in background concentrations [9]. Background CO concentrations can be investigated through the greenhouse gas monitoring network established by the Global Atmospheric Watch Program of the World Meteorological Organization (WMO/GAW), in collaboration with multiple countries [10–13]. China contributes to WMO/GAW with four background stations: Mt. Waliguan in Qinghai Province (WLG, global background), Shangdianzi in Beijing (SDZ, regional background), Longfengshan in Heilongjiang Province (LFS, regional background), and Lin'an in Zhejiang Province (LAN, regional background). Located in rural areas, these stations conduct long-term greenhouse gas observations and are managed by the China Meteorological Administration (CMA). The continuous background CO observations could reflect the differentiation between natural variations and anthropogenic activities impacting CO concentrations and the influence of long-distance transport. By identifying sources and sinks and analyzing long-range transport impacts, decision-makers could develop strategies to mitigate CO emissions and manage regional cross-boundary pollution [14,15]. Hence, CO monitoring could support climate action, improve our understanding of the overall carbon cycle, improve urban air quality, and enhance public health, all of which are vital for sustainable development.

As one of the most densely populated regions in the world, rapid economic development and population growth in the Yangtze River Delta (YRD) region have led to significant anthropogenic CO emissions. Long-term CO observations at LAN in the YRD region have recorded almost the highest CO concentrations among regional background stations in China [7,16,17]. Liu et al. [17] concluded that the multi-year average concentration of CO from 2010 to 2017 was 372.5 ± 0.6 ppb at LAN, coinciding with the high CO column concentrations remotely sensed in the YRD region [18]. Short-time observations at some urban stations of the YRD were even more than twice as high as at LAN. For example, the annual average CO concentration at an urban station in Nanjing was reported to reach 757.5 ± 410.5 ppb [19], while in Shanghai, it reached around 823 ppb [20]. Although there are significant differences in CO levels between these urban sites and the LAN station, the diurnal variation at LAN exhibited a bimodal pattern similar to urban stations, unlike other background stations [7,16,17]. This bimodal pattern, coinciding with commuter rush hours, suggested that LAN is significantly affected by local anthropogenic emissions [7]. The intensified anthropogenic impacts on LAN could reduce its spatial representativeness.

Furthermore, in the literature, few researchers paid attention to quantifying background observation sites' spatial representation scale.

Before utilizing observation data from background stations, it is a critical and fundamental step to evaluate the extent to which these observation data accurately reflect the conditions of the surrounding area. The most widely employed approach involves statistical analyses, which compare ground-based observations with broader regional datasets to quantify representativeness. For instance, Martin et al. [21] utilized WRF-CHIMERE simulations in conjunction with station observation records, and if the differences between the two datasets remained within a specified percentage, the observation records could be regarded as a good spatial representative. Vitali et al. [22] applied a Lagrangian model to simulate the PM₁₀ diffusion patterns and employed a concentration similarity frequency function to analyze time-series simulation, verifying the spatial representativeness of air quality monitoring stations situated in an industrial zone. Furthermore, advancements in remote sensing and reanalysis datasets provide additional tools for evaluating the representativeness of ground-based observations. The high spatial resolution offered by these datasets allows for a more detailed comparison of localized station measurements with larger regional or global atmospheric conditions [23].

This study focused on a new regional background station in the YRD, the Damingshan Station (DMS), which is located at the mountaintop of Morning Glory in Lin'an County, Zhejiang Province. As a high-altitude station (1483 m a.s.l.) in the YRD region, the air at the site is well mixed, and there is no obvious source of anthropogenic pollution, making it an ideal regional observation site. The objectives of this study are: (1) to assess the spatiotemporal characteristics of CO based on the first continuous observation of CO at DMS; (2) to quantify the spatial representation of DMS combined with atmospheric composition reanalysis data. The findings of this study could provide more accurate background information of CO for the largest economically developed zone in the world and offer scientific evidence for air pollution management and CO emission control measures.

2. Methodology

In this study, the first continuous observations of CO at DMS were analyzed to assess spatiotemporal characteristics and impact factors. Furthermore, CAMS (The Copernicus Atmospheric Monitoring Service Reanalysis Data) was applied to aid in quantifying the spatial representation of the regional background station. The flowchart of this study is as follows (Figure 1).

2.1. Monitoring Site

The CO concentrations were monitored at a meteorological station on the summit of Morning Glory (DMS) in the northwest of Zhejiang Province (Figure 2). Morning Glory is located at the junction of Zhejiang Province and Anhui Province and is a part of the southwest extension of the Tianmu Mountains, with higher terrain to the northwest and lower terrain to the southeast. DMS (30°01' N, 119°00' E) is adjacent to the economically developed YRD region and about 1400 m higher than the average sea level of the YRD (<100 m). DMS is approximately 270 km southwest of Shanghai, 110 km from Hangzhou, and 50 km from LAN. No villages or factories are within a 2 km radius of the station. All of these factors made the DMS an ideal regional observation site.

The region transitions from the subtropical to the north subtropical zone. Influenced by topography and climate, it manifests a warm and humid maritime climate punctuated by strong monsoons, distinct seasons, mild temperatures, ample rainfall, and abundant sunlight. Rapid elevation changes engender significant climatic diversity, resulting in distinct vertical boundaries in vegetation distribution. From the foothills to the mountaintop,

the vegetation progresses: below 870 m is a zone of evergreen broadleaf forest; from 870 to 1100 m is a zone of mixed evergreen and deciduous broadleaf forests; from 1100 to 1380 m is a zone of deciduous broadleaf forests; and from 1380 to 1506 m is a zone of deciduous dwarf forests [24].

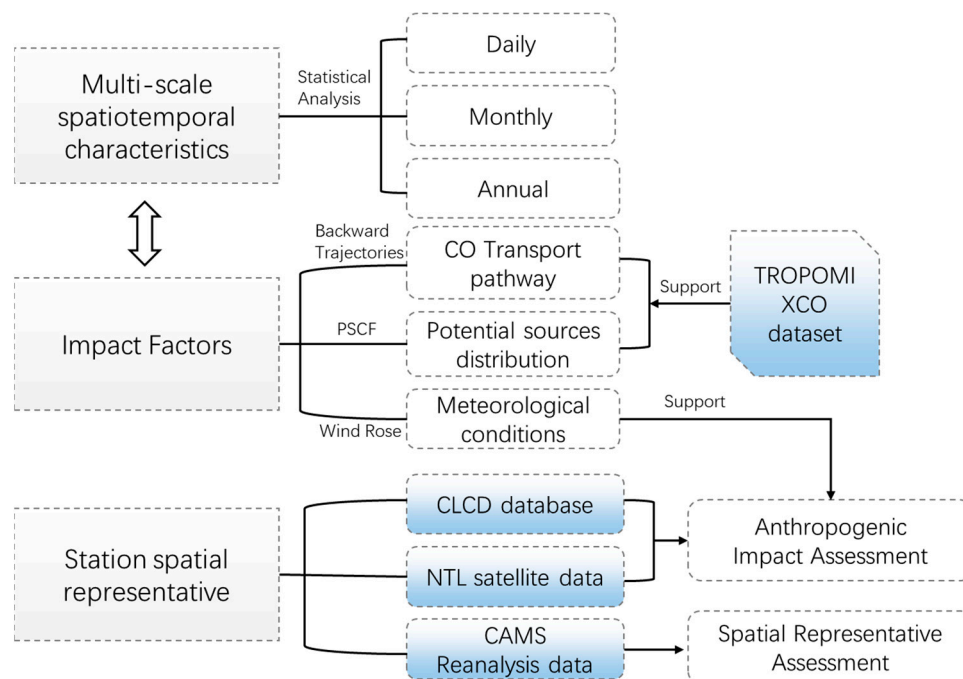


Figure 1. Research flowchart of this study.

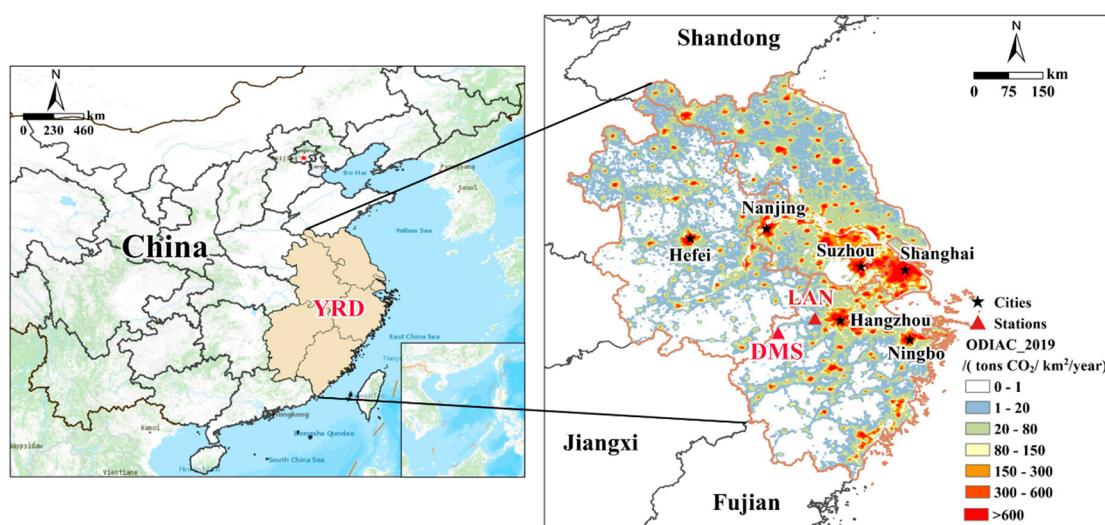


Figure 2. Left: The location of the YRD region in China. Right: The distribution of metropolises and the location of DMS and LAN in YRD. The base map on the right was from the Open-source Data Inventory for Anthropogenic CO₂ (ODIAC) data in 2019, downloaded via <https://db.cger.nies.go.jp/dataset/ODIAC/> accessed on 14 August 2024.

2.2. Measurement System

Atmospheric CO was observed continuously by a cavity ring-down spectrometer (G2401, Picarro, Inc., Santa Clara, CA, USA) at DMS from September 2020 to January 2022. Figure 3 shows the workflow of the measurement system at DMS. The ambient air was pumped into the instrument by a vacuum pump (N022, KNF Neuberger, Freiburg im Breisgau, Germany) for analysis through a 10 mm O.D. sampling line (Synflex 1300 tubing; Eaton, OH, USA) positioned 10 m above ground level outside the experimental

square cabin (Figure 4). The air was then directed to a glass trap (MC480D1, SP Industries, Warminster, PA, USA) submerged in a methanol bath at $-50\text{ }^{\circ}\text{C}$ and dried to a dew point of approximately $-35\text{ }^{\circ}\text{C}$.

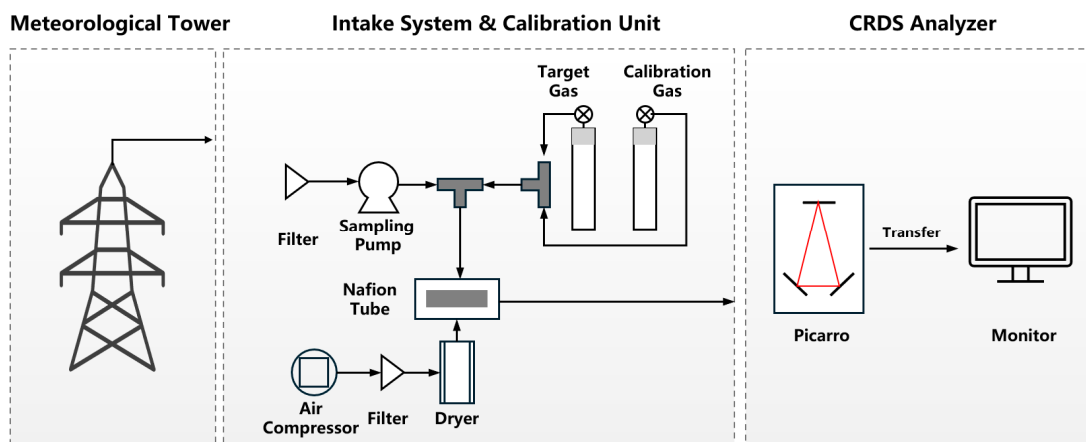


Figure 3. Schematic of the measurement system at DMS.



Figure 4. DMS at the hilltop flat. (a): Experimental square cabin on the summit of DMS; (b): a 10 mm O.D. sampling line outside the experimental square cabin at the top of a 10 m tower.

Calibration of the measurements was conducted using calibration gases with known concentrations (S). To ensure precision and accuracy, a target gas (T) with a known CO concentration was routinely analyzed. The S and T were pressurized into 29.5 L treated aluminum alloy cylinders, which can be scaled to the WMO X2014A standard. The calibration process is scheduled with 8 h sample air, then 5 min calibration gas, followed by another 8 h sample air, and 5 min target gas. A linear fitting approach was applied for CO calibration using the nearest calibration gas measurements. Detailed information about the system is provided by Fang et al. [25], and it has been demonstrated that the instrument and measurement technique are suitable for high-precision CO measurements in ambient air [26].

According to the User's Guide provided by Picarro, the measurement precisions of the instrument for CO are 15 ppb, 1.5 ppm and 1 ppb in 5 s, 5 min and 60 min, respectively. The measurement uncertainty of the Picarro instrument at DMS is calculated as the standard deviation of T, and the maximum uncertainty is less than 2 ppb for CO measurement. This level of precision and accuracy meets the WMO data quality targets for GAW stations.

According to Figure 4, DMS is situated at a hilltop flat with sparse tall trees. The hilltop flat stands more than 15 m above the nearest tree canopy, ensuring that the CO sampling inlet, positioned at the top of a 10-m tower, is more than 25 m above the tree

canopy. Furthermore, the wind speed and wind direction sensors are installed at the top of the same tower. This setup ensures that the CO concentration measurements are synchronized with wind speed and direction observations.

Meteorological parameters, such as wind speed and direction, were obtained from the Hangzhou Meteorological Bureau. The observation equipment for these parameters underwent annual calibration and testing to ensure accuracy. All data used in our analysis were collected using well-calibrated instruments, following the ground observation protocols of the China Meteorological Administration. Additionally, we excluded data points with wind speeds below 0.1 m/s during winter months to account for potential equipment freezing issues. This step was crucial to maintain the integrity and accuracy of our dataset before proceeding with further data processing.

2.3. Data Analysis

2.3.1. Data Filter

A rigorous quality control process of all observation records was conducted prior to the data analysis. The data marked with equipment failure or instrument maintenance were first excluded for further analysis. After the quality control process, the data were averaged by hours, and there were consequently 10,361 pieces of hourly CO records (92.8% of the total records), also flagged as regional representatives at DMS in this study. And 801 pieces of hourly CO records (7.2% of the total) were excluded due to outliers from instrument calibration and malfunctions. Figure 5 shows the filtered regional CO concentrations at DMS during the study period. The high values of CO concentration were mainly distributed in spring and winter, with lower values of CO concentration in summer.

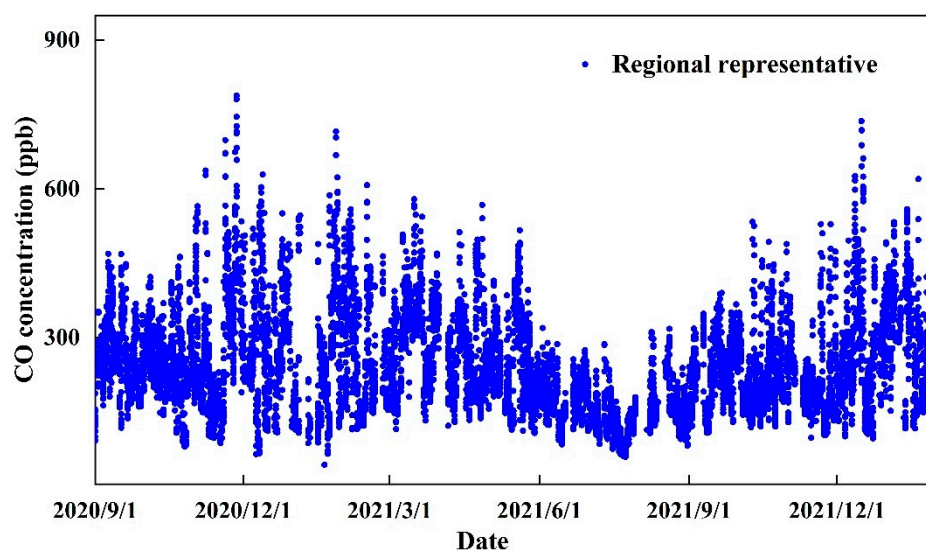


Figure 5. Hourly CO data series at DMS station during the study period.

2.3.2. Atmospheric Transport Model

To understand the influence of atmospheric transport, the Hybrid Single-Particle Lagrangian Integrated Trajectory (HYSPLIT) dispersion model was employed in this study. Air mass back trajectories for this study using gridded meteorological data (GDAS $1^\circ \times 1^\circ$ data from 2020 to 2022) provided by the National Oceanographic and Atmospheric Administration (NOAA). The 1-day air mass back trajectories could cover the YRD region well, enabling us to examine regional transportation dynamics within the YRD. Regarding previous literature, the 3-day air mass back trajectories were widely used to figure out the impacts of long-distance transportation on the station in YRD. Both 1-day and 3-day backward trajectories are calculated in this study.

2.3.3. Potential Sources Contribution Function

The Potential Sources Contribution Function (PSCF) model was used in this study to analyze potential source regions of CO for DMS. The average weighted value was calculated in a $1.0 \times 1.0^\circ$ degree grid cell (i, j) as follows:

$$PSCF_{ij} = m_{ij}/n_{ij} \quad (1)$$

n_{ij} represents the number of endpoints passing through the ij grid cell, and m_{ij} represents the number of trajectories with CO concentration exceeding the seasonal average value [27]. The weighted PSCF model (WPSCF) can help us better understand the source of atmospheric CO at DMS in this study, which can be used in the software application named TrajStat [28]. $PSCF_{ij}$ was calculated using the following random measure of W_{ij} to reduce the anomalous effect of small n_{ij} values in some cells. N_{ave} represents the average number of the endpoints of the total cells.

$$W_{ij} = \begin{cases} 1.00, & 3n_{ave} < n_{ij} \\ 0.70, & 1.5n_{ave} < n_{ij} < n_{ave} \\ 0.42, & n_{ave} < n_{ij} < 1.5n_{ave} \\ 0.05, & n_{ij} < n_{ave} \end{cases}$$

To study the contribution of regional sources to the recorded CO concentrations, TrajStat plug-in in the MeteInfo was applied. The 1-day and 3-day back trajectories consistent with the hourly observations were calculated and clustered at the site, and the arrival height of the trajectories was set to 500 m a.g.l. The base maps of back trajectory maps, showing the average CO total column mixing ratio, were observed by the TROPOspheric Monitoring Instrument (TROPOMI) on the Sentinel 5 Precursor (S5P) satellite. Seasonal trajectories were calculated for the CO concentrations tagged as regional representatives.

2.3.4. Spatial Representative

The CAMS reanalysis is a global reanalysis dataset for atmospheric composition, including aerosols, chemical species, and greenhouse gases produced by the European Center for Medium-Range Weather Forecasts (ECMWF) (data source: <https://ads.atmosphere.copernicus.eu/cdsapp#!/dataset/cams-global-reanalysis-eac4?tab=form> accessed on 11 June 2024) [29,30]. CAMS has been extensively evaluated and applied in various studies [30,31]. For CO, CAMS demonstrated an excellent representation of seasonal cycles and inter-annual variability and was in good agreement with CO observations of Total Carbon Column Observing Network stations (TCCON) [29]. The Comprehensive Evaluation and Quality Assurance (EQA) reports from CAMS have facilitated comparisons between CO reanalysis data and in situ observations from monitoring sites managed by the China National Environmental Monitoring Centre. These reports indicated strong correlations between CAMS and surface observations across numerous stations in China. Specifically, CAMS CO values closely match observed values in the YRD regions, where monitoring sites exhibited lower modified normalized mean biases (MNMBs) and higher correlations compared to the national average [32,33]. These findings underscore the accuracy of CAMS in representing CO concentrations in the YRD region. This study used the CAMS global reanalysis CO dataset with a spatial resolution of $0.75^\circ \times 0.75^\circ$ and 3-hourly temporal resolution from September 2020 to January 2022 to study the representativeness of CO observations at DMS.

A total of 14 buffer zones centered on DMS were delineated at a 0.75° resolution increment, and the average CO of CAMS in 14 buffers was calculated to represent the average CO concentration for each buffer area with a temporal resolution of 3 h. The average CO concentration of CAMS served as a representative value for average CO levels

within each buffer zone. Every 3-h mean and the standard deviations were also calculated for the in situ CO observation records at DMS, and then the results were compared with corresponding CAMS averages. For every buffer, comparisons were conducted for every 3-h mean. The well-represented percentage is calculated as follows:

$$\text{well-represented percentage} = \frac{\text{COUNT}\left(\left| \text{mean}_{3h}^{\text{CAMS}} - \text{mean}_{3h}^{\text{DMS}} \right| \leq \text{SD}_{3h}^{\text{DMS}}\right)}{\text{COUNT}\left(\text{mean}_{3h}^{\text{DMS}}\right)}$$

where $\text{mean}_{3h}^{\text{CAMS}}$ is the average of CAMS data with 3 h intervals, $\text{mean}_{3h}^{\text{DMS}}$ is average of DMS observation records with 3 h intervals, and $\text{SD}_{3h}^{\text{DMS}}$ is the standard division of DMS observation records with 3 h intervals.

The higher well-represented percentage referred to better representing the CO observations at DMS for the corresponding buffer.

2.4. Other Datasets

2.4.1. Land-Use and Land-Cover Information

The annual China Land Cover Dataset (CLCD) database, containing land-use and land-cover information around DMS and LAN, was applied in this study. CLCD was the first Landsat-derived annual dataset for Chinese land use and land cover, with 30 m spatial resolution spanning from 1990 to 2021 [34]. The dataset can be downloaded via the website (<https://zenodo.org/record/4417810#.YnYXLlxBw2y> accessed on 7 July 2024). Land use and land cover could be regarded as a surrogate of local human activity intensity, as a high fraction of anthropogenic and semi-anthropogenic ecosystems (e.g., impervious surface and cropland) is typically associated with intensive human activities, whereas natural ecosystems (e.g., forest and shrub) are less impacted. The CLCD data of 2021 was utilized to compare land-use and land-cover information within a 20 km radius around DMS and LAN according to main categories: cropland, forest, shrub, grassland, water, and impervious. This comparison aimed to assess the local anthropogenic influences on the observatories at both sites.

2.4.2. Nighttime Light Intensity Information

The Nighttime Light (NTL) satellite data in 2021, provided by the Yangtze River Delta Science Data Center, was used in this study [35]. The dataset can be downloaded via the website (<http://geodata.nnu.edu.cn/> accessed on 6 August 2022). NTL data are often used to characterize urbanization, socioeconomic development, and human activities, as they are closely related to human production and living footprints [36–38]. The NTL intensity maps were drawn with a 20 km buffer around DMS and LAN in our study to analyze the urban structure and urban development around the two sites.

3. Results and Discussions

3.1. Different Temporal Variation of Observation Records at DMS

3.1.1. Annual Average Concentration of CO

The annual average concentration of CO at DMS was compared to other observation sites in Asia (Table 1). The regional representative at DMS showed an annual average CO concentration of 233.4 ± 3.8 ppb, which was about 2.45 times higher than the global average of 95 ± 3 ppb in 2021 [39]. According to Table 1, the YRD region had relatively higher CO background concentration (372.5 ± 0.6 ppb at LAN and 233.4 ± 3.8 ppb at DMS) compared to the other regional background stations in Asia (Shangdianzi: 159.4 ± 0.4 ppb, Longfengshan: 199.9 ± 0.9 ppb, Gosan: 190.1 ± 49.5 ppb, Yonagunijima: 140.0 ± 41.2 ppb). The concentration was also higher than those observed at Mt. Waliguan, the global back-

ground station in China (110.7 ± 0.2 ppb). LAN was designed to catch the dynamic changes of atmospheric background components in the YRD [40]. However, with the extensive development of Lin'an County and the YRD region, LAN was significantly affected by anthropogenic emissions such as vehicle emissions, biofuel burning, biomass burning, and industrial emissions near the station [41]. Its observations were even 2.33 times higher than those at the Shangdianzi station near the Chinese capital (Beijing), another atmospheric regional background monitoring site for the Beijing-Tianjin-Hebei megacity region. The elevated emissions from the surrounding anthropogenic sources potentially narrowed LAN's regional representativeness, limiting its ability to reflect broader trends within the YRD region.

Table 1. Average CO concentrations of DMS and other Asia sites.

Site	Lat. (°N)	Lon. (°E)	Altitude (m a.s.l)	Time of Observation	Average CO Concentration	Reference
DMS China	30.01	119.00	1483	September 2020–January 2022	233.4 ± 3.8 ppb	This study
Lin'an (LAN) China	30.18	119.44	138	September 2010–May 2017	372.5 ± 0.6 ppb	[17]
Lulin China	23.47	120.87	2862	April 2006–April 2011	129.3 ± 46.6 ppb	[42]
Taiwan Mt. Waliguan China	36.28	100.89	3810	2019	110.7 ± 0.2 ppb	[16]
Shangdianzi China	40.65	117.12	293.3	December 2011–May 2017	159.4 ± 0.4 ppb	[17]
Longfengshan China	44.44	127.36	330.5	January 2017–November 2019	199.9 ± 0.9 ppb	[43]
Shangri-La China	28.01	99.73	3580	2013	109.0 ± 1.0 ppb	[15]
Akedala China	47.10	87.93	563.3	September 2009–December 2019	158.0 ± 13.4 ppb	[44]
Gosan South Korea	33.28	126.17	71.3	May 2012–April 2015	190.1 ± 49.5 ppb	[45]
Yonagunijima Japan	24.47	123.02	30	2004	140.0 ± 41.2 ppb	[46]

Both LAN and DMS are located in Lin'an County, Hangzhou, with the straight-line distance between the two being close to 75 km. In comparison to LAN, the annual mean CO concentration at DMS was notably 37.34% lower. DMS had a higher altitude and was further away from population centers and industrial agglomeration, leading to much lower CO concentration observed at the site. Hence, DMS may provide a more accurate description of spatiotemporal changes in regional CO concentration within the YRD region. Although DMS was less affected by local emissions, it continues to show elevated CO levels compared to other Asian sites. This persistent elevation in CO concentration could be attributed to the influence of atmospheric transportation within the YRD region, one of the most developed megacity clusters in the world.

3.1.2. Seasonal Characteristics

Figure 6 shows the monthly variations of CO concentrations to better understand the seasonal characteristics of CO at DMS. The highest seasonal CO concentrations were 290.5 ± 4.3 ppb observed in winter (DJF: Dec., Jan., Feb.), followed by 276.6 ± 4.0 ppb observed in spring (MAM: Mar., Apr., May.), 247.3 ± 2.8 ppb in autumn (SON: Sep., Oct., Nov.), and the lowest CO concentrations were 158.9 ± 2.3 ppb observed in summer (JJA: Jun., Jul., Aug.). Similar seasonal CO cycles have been reported in many other sites in the NH, such as Gosan [45], LAN [7], and Akedala [44].

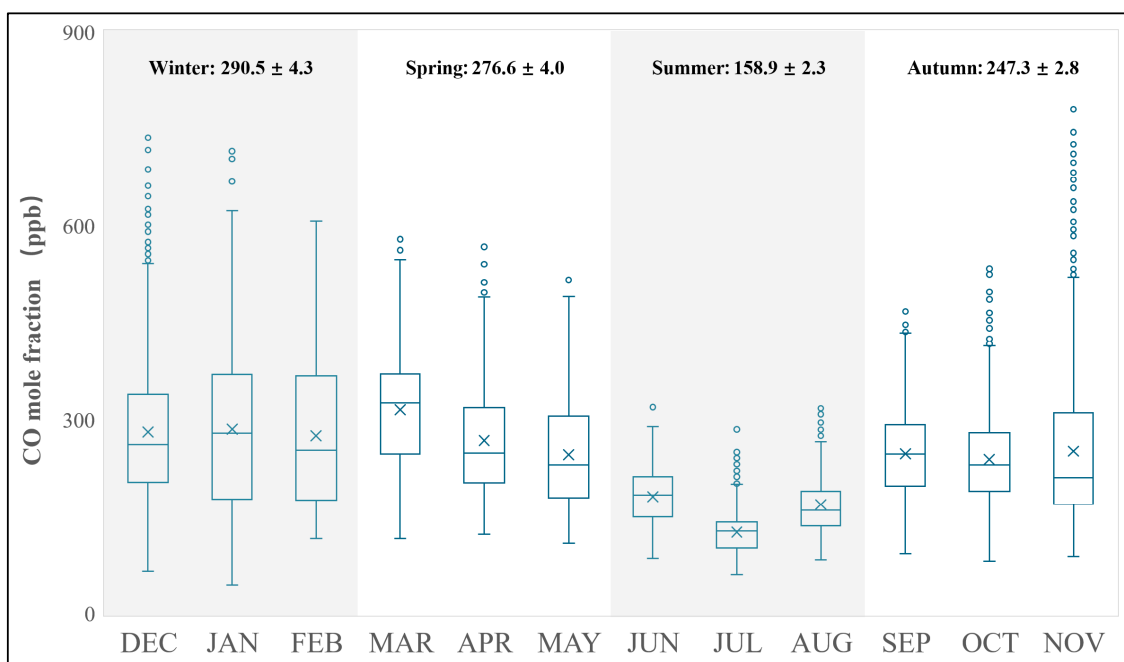


Figure 6. Monthly statistics of CO concentrations at DMS during the study period. The lines in the box are the median CO concentrations; the bottom and the top of the box represent the 25th and the 75th percentile; the bottom whisker reaches the minimum, and the top whisker extends 1.5 times the Interquartile Range (IQR); the crosses are the average monthly CO concentrations; the blue dots are the outliers.

Although the winter average was slightly higher than the spring, the highest monthly CO level was observed in March (313.8 ± 6.4 ppb). The lowest monthly CO level was observed in July (128.7 ± 2.8 ppb). The bird's-eye view from the Measurement of Pollution in the Troposphere (MOPITT), launched by NASA, also detected climbing average levels of CO in spring over East China during 2003–2007 [47]. Elevated CO levels in spring were usually discovered at the coastal sites in East Asia, coinciding with the Asian continental outflows [42,48,49], unlike sites in the inner Asian continent, such as Akedala [44] and SDZ [50]. Previous studies have shown that surging energy consumption during heating seasons brought additional air pollutants (e.g., ozone, CO, aerosols) to South China. These pollutants were carried by the winter monsoon, which also drove Asian continental outflows originating in inland China to the south coastal regions in springtime [51,52]. Besides, according to the MOPITT observation and STEM simulation (a regional chemical transport model), biomass burning from Southeast Asia may contribute to the CO enhancement in spring. These CO can diffuse to the west coast of the Pacific, including the regions from Hong Kong to Taiwan [42,47]. During the summer, airflow from the Pacific Ocean dominates the surface and free troposphere in East Asia. The presence of a large number of OH radicals due to increased ultraviolet (UV) radiation resulted in the lowest seasonal CO levels over the Yangtze River Delta (YRD) [51,53]. Higher air temperatures in summer also contributed to increased atmospheric turbulence, enhancing horizontal transport and vertical diffusion of pollutants compared to other seasons.

Figure 6 further implies the hourly average CO concentration data distribution for all seasons. In winter, the CO data (DJF) showed a much more extensive distribution than those of the other three seasons, particularly summer (JJA). The standard deviation of CO concentration in winter was 123.5 ppb, while that in summer was 44.2 ppb. However, similar characteristics were not found in long-term observations at LAN, and the summer distribution was not substantially narrower than that of winter [7]. Compared to LAN, the CO data at DMS showed better thoroughly mixed weather conditions and

less impact from the local release sources during summertime (further analysis shown in Sections 3.2 and 3.3). In contrast, the winter data may be more sensitive to different release sources, including local sources and long-distance transportation pollutants, due to the directional switch of the winter monsoons.

3.1.3. Diurnal Cycle

Figure 7 depicts the diurnal cycles of CO concentrations observed at DMS. The diurnal variations in CO consistently exhibited analogous patterns throughout all seasons, characterized by nocturnal peaks between 17:00–21:00 LT (local time) and morning valleys occurring between 05:00–09:00 LT. This diurnal pattern was similar to other high-altitude stations, such as Lulin [42], Mt. Huang [54], and Mount Tai [55], except that the peak time was postponed from 13:00–15:00 LT to 17:00–21:00 LT.

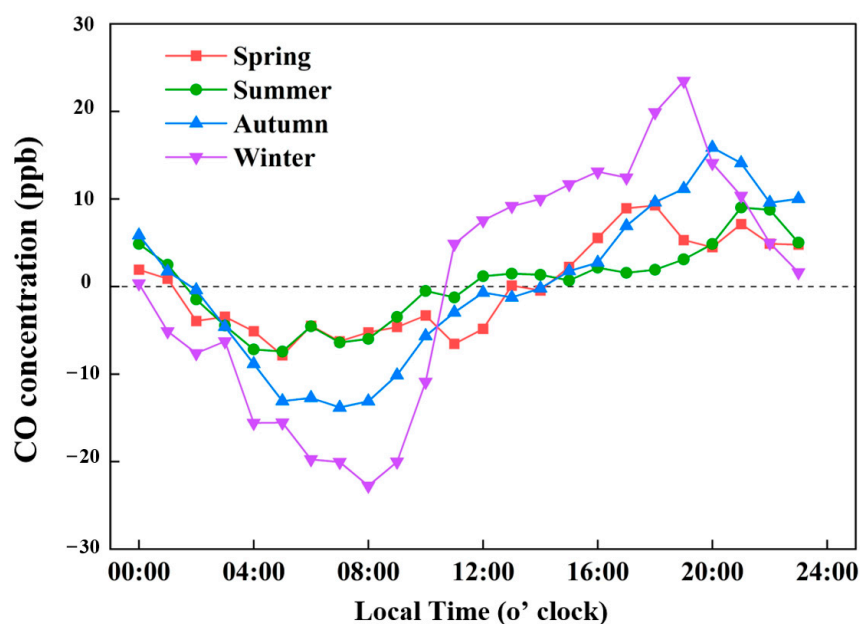


Figure 7. Anomaly diurnal circle of CO concentrations at DMS during the study period. Spring: March to May; summer: June–August; autumn: September–November; winter: December–February.

However, near-ground stations in the YRD region showed a bimodal distribution of CO concentrations influenced by urban rush hours. These stations recorded the lowest concentrations between 12:00 and 16:00 LT. Examples include stations in Lin’an [7], Nanjing [19], and Shanghai [20]. According to our preview study, the DMS is a high-altitude station. The height of the Planetary Boundary Layer (PBL) was usually lower than the DMS’s altitude at night, restricting the vertical spread of CO to DMS [56]. Consequently, the air surrounding the station was cleaner during 22:00–07:00 LT. As temperatures rise after sunrise, the PBL height expands, aided by upslope winds and sea breezes, facilitating the upward movement of CO and causing a noticeable increase in CO concentrations during the daytime.

Contrary to the typical diurnal pattern observed in previous literature, where CO concentrations peaked in the afternoon (14:00–16:00 LT), CO levels at DMS either continued to rise or remained high during the afternoon and early evening hours due to atmospheric transport within the YRD region. Compared with other high-altitude stations [42,54,55], the afternoon CO elevation varied by season. The observed CO values during 14:00 to 18:00 LT in spring, 16:00 to 22:00 LT in summer, 16:00 to 20:00 LT in autumn, and 14:00 to 19:00 LT in winter were selected based on these afternoon growths to draw the 1-day back trajectories (Figure 8) and compare them with the 1-day back trajectory maps of the whole day records (Figure 9).

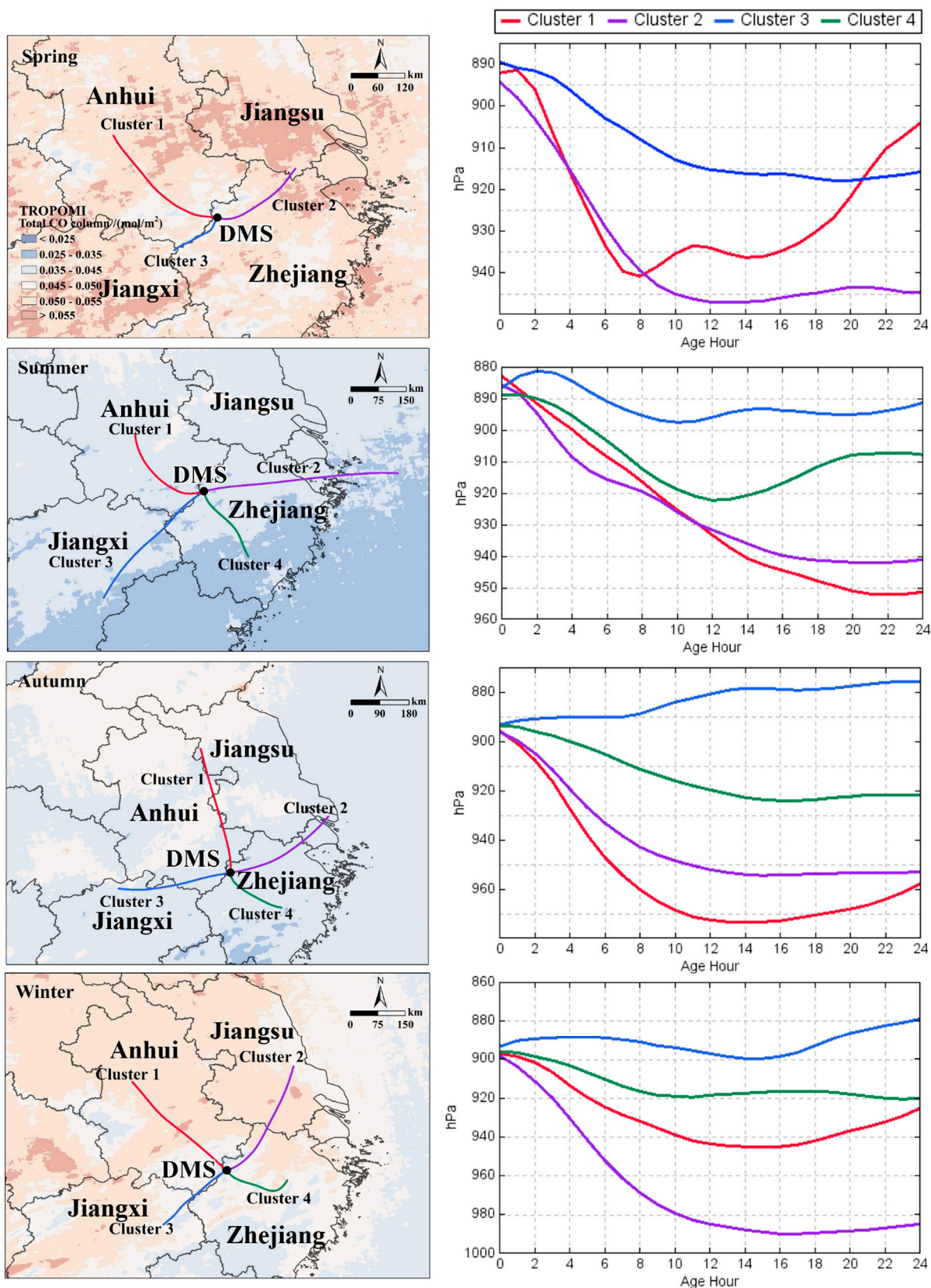


Figure 8. Left: Cluster analysis of 1-day back trajectories for the most significant concentration enhancement period of the whole day (14:00–19:00 LT in spring, 16:00–22:00 LT in summer, 16:00–20:00 LT in autumn, 14:00–19:00 LT in winter) at DMS. Right: The average pressure changes corresponding to each cluster. The colorful lines on the map are cluster analysis results with base maps of average column CO concentration retrieval from TROPOMI products.

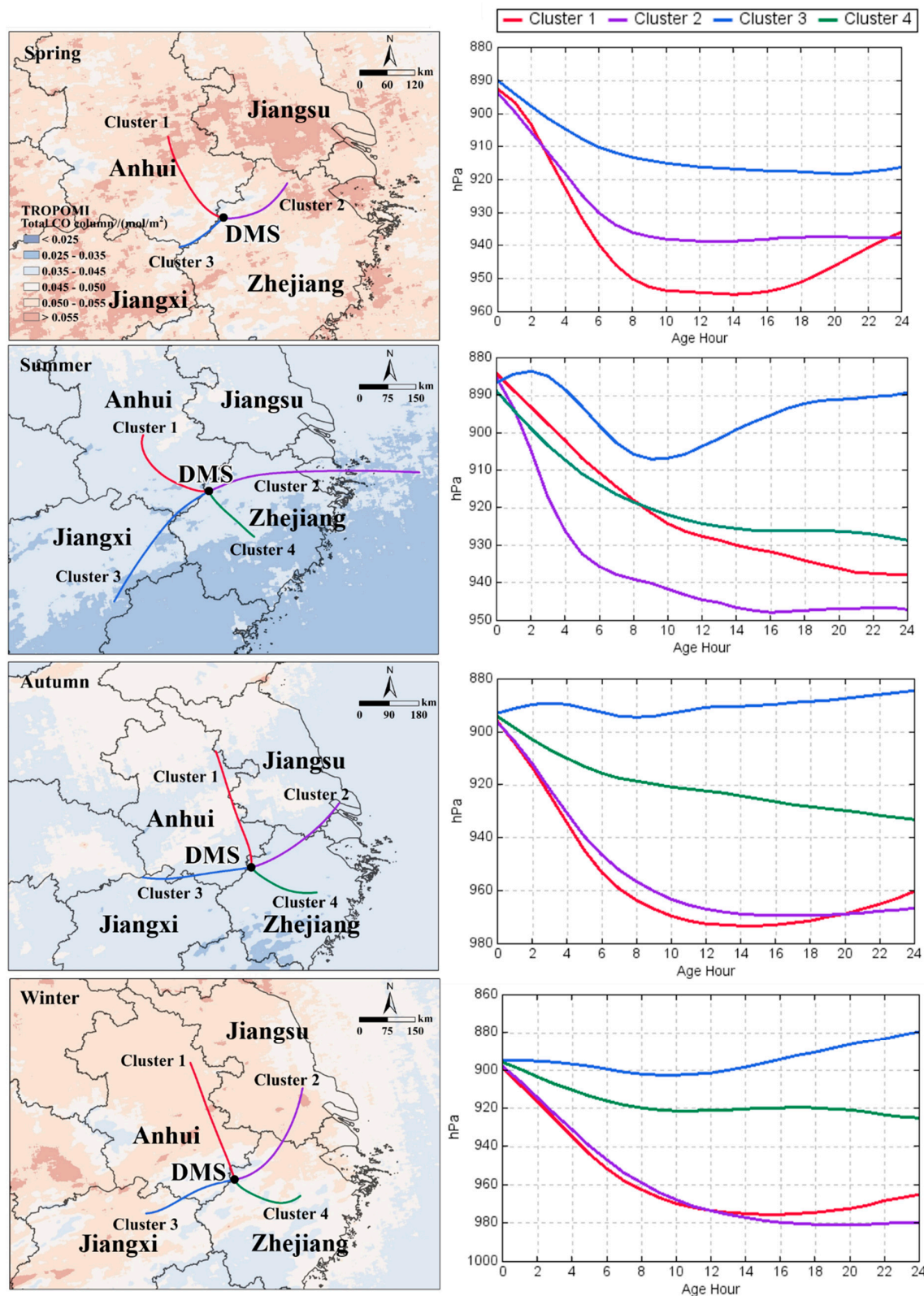


Figure 9. Left: Cluster analysis of 1-day back trajectories encompassing all seasons from 2020 to 2022 at DMS. The colorful lines on the map are cluster analysis results with base maps of average column CO concentration retrieval from TROPOMI products. Right: The average pressure change corresponds to each cluster.

The percentage of the trajectories from the northeast (Cluster 2), where the primary megacities of YRD were situated, increased significantly during the afternoon. Elevated

CO levels accompanied those increased trajectory percentages in Figure 8, compared to the concentration averages of the corresponding clusters in Figure 9. The trajectories of Cluster 2 remained close to the ground surface, making them more susceptible to anthropogenic CO emissions from the YRD region. Also, the air masses from the north and passing through the Hefei metropolitan area (Cluster 1) experienced higher CO levels in the afternoon. Hence, the afternoon CO elevation could be associated with atmospheric transport and discharge from the YRD urban areas.

3.2. Influence of Atmospheric Transport and Potential Sources Contribution

As shown in Figure 9 and Table 2, the 1-day back trajectories covered the YRD regions in all directions, with air masses from the northeast accounting for significant proportions: 32.7% in spring, 24.9% in summer, 40.8% in autumn, and 33.8% in winter. These air masses, originating close to the ground, passed through several major metropolitan areas, including Shanghai, Hangzhou, and Suzhou, where intense anthropogenic emissions could be transported to the DMS site. After approximately 16 h of transport, these air masses ascended along the mountains, bringing elevated CO levels to DMS. The air masses from the north always carried the highest CO concentrations in spring, autumn, and winter, roughly corresponding to the winter monsoon in East Asia. Moreover, a substantial portion of air mass originated from the southwest and southeast and traversed the inland areas of the YRD, carrying comparably low levels of CO concentration. Those areas were expansively covered by mountains and forests and dotted with sporadic towns/cities. As a result, the air masses from the south are consistently transported at relatively higher altitudes compared to Cluster 1 and Cluster 2. Those findings were also supported by Liu’s work at the LAN station [17].

Table 2. The statistics of the cluster analysis at DMS.

Cluster		Average CO (Unit: ppb) (Percentage)		
		Figure 9: 1-Day	Figure 10: 3-Day	Figure 8: Specified Time
Spring	1	326.3 ± 12.6 (15.9%)	285.0 ± 8.8 (25.1%)	355.0 ± 26.9 (15.8%)
	2	290.0 ± 8.0 (32.7%)	302.1 ± 8.4 (35.6%)	296.4 ± 16.6 (37.9%)
	3	264.8 ± 5.9 (51.4%)	266.8 ± 6.8 (39.3%)	262.4 ± 13.0 (46.3%)
Summer	1	157.7 ± 6.2 (10.6%)	162.9 ± 6.0 (13.9%)	159.7 ± 14.9 (11.0%)
	2	138.6 ± 7.3 (24.9%)	156.5 ± 6.2 (28.9%)	157.8 ± 14.2 (29.5%)
	3	149.5 ± 2.9 (34.2%)	147.9 ± 2.5 (35.9%)	151.6 ± 4.9 (34.6%)
	4	170.6 ± 3.7 (30.4%)	164.9 ± 4.7 (21.4%)	169.4 ± 7.6 (24.8%)
Autumn	1	279.3 ± 7.8 (22.0%)	288.0 ± 6.0 (29.1%)	288.1 ± 12.6 (24.1%)
	2	250.1 ± 4.1 (40.8%)	244.8 ± 4.7 (25.7%)	258.5 ± 6.2 (45.6%)
	3	206.8 ± 7.8 (7.0%)	225.1 ± 6.9 (15.4%)	213.5 ± 14.2 (7.2%)
	4	223.0 ± 3.8 (30.2%)	216.0 ± 3.7 (29.8%)	228.7 ± 6.3 (23.1%)
Winter	1	321.5 ± 11.2 (25.3%)	299.2 ± 9.4 (29.3%)	329.6 ± 18.6 (28.2%)
	2	270.6 ± 7.3 (33.8%)	280.2 ± 8.6 (27.2%)	293.1 ± 14.5 (35.9%)
	3	278.2 ± 8.6 (20.3%)	286.9 ± 8.1 (25.4%)	307.1 ± 24.1 (10.1%)
	4	260.9 ± 7.2 (20.7%)	252.7 ± 7.7 (18.1%)	280.7 ± 12.0 (25.9%)

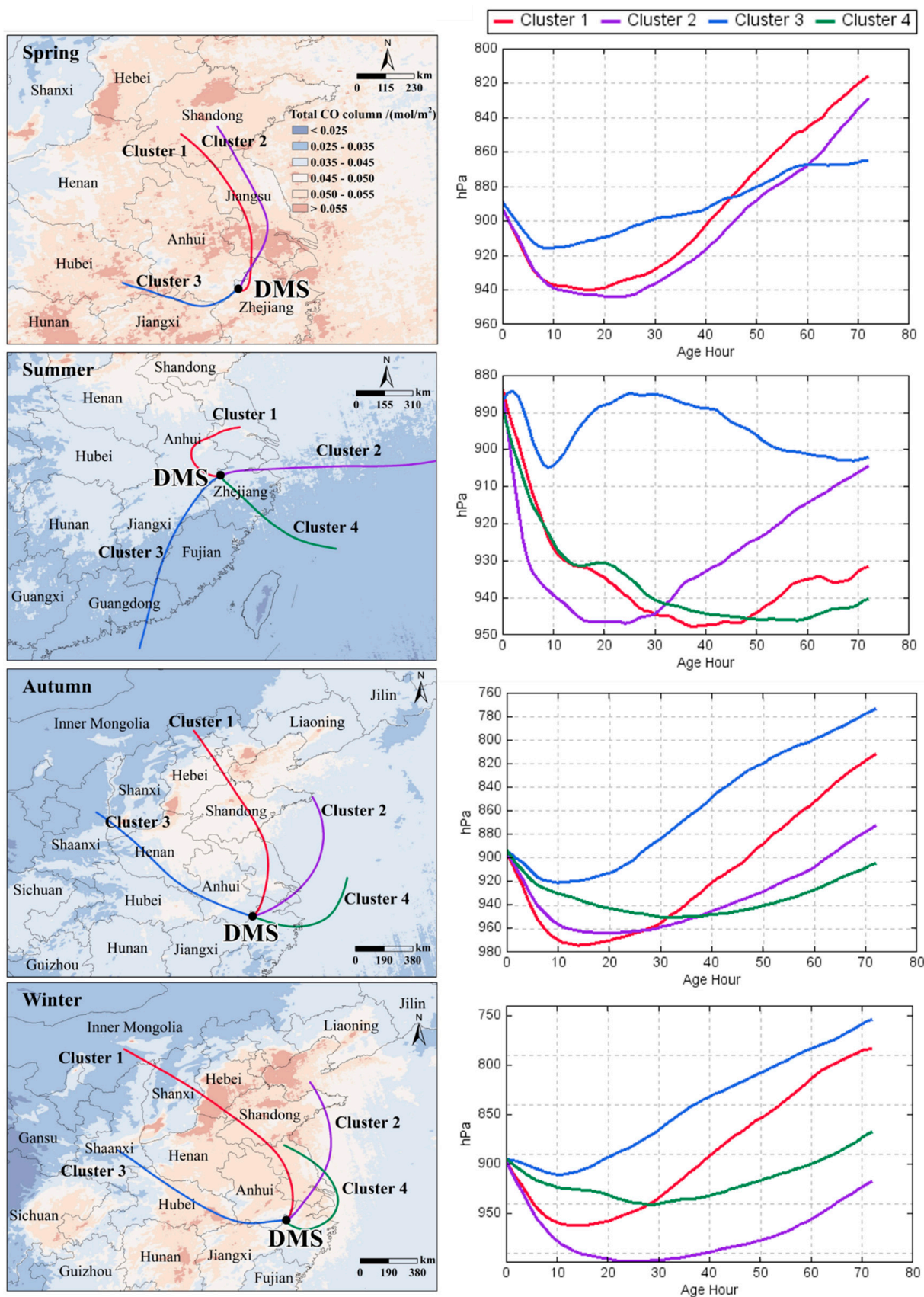


Figure 10. Left: Cluster analysis of 3-day back trajectories encompassing all seasons from 2020 to 2022 at DMS. The colorful lines on the map are cluster analysis results with base maps of average column CO concentration retrieval from TROPOMI products. Right: The average pressure change corresponds to each cluster.

Figure 10 shows the long-distance atmospheric transport reaching DMS. Our results showed that the air masses from the north significantly impacted the CO levels at the monitoring site, except during the summer season. In spring, the air masses from the northeast and the north (Cluster 1 + 2, accounting for around 60.7% of the total trajectories) brought a higher CO concentration, exceeding 20 ppb compared to those from the western regions (as shown in Table 2). The regional YRD emissions contributed to the elevated CO levels in the spring, supported by shorter trajectories and high WPSCF values in the YRD (Figures 10 and 11). The northern areas, including Beijing, Hebei, and Shandong provinces, were identified as high-potential sources during spring. Furthermore, regions with high potential emissions were also observed in Hubei, Guizhou, Yunnan, Hunan, and Guangxi provinces, with an extended influence reaching the boundaries between China and India. The analysis suggested that while YRD emissions significantly influenced CO concentrations at DMS, long-distance transport also brought emissions from remote regions.

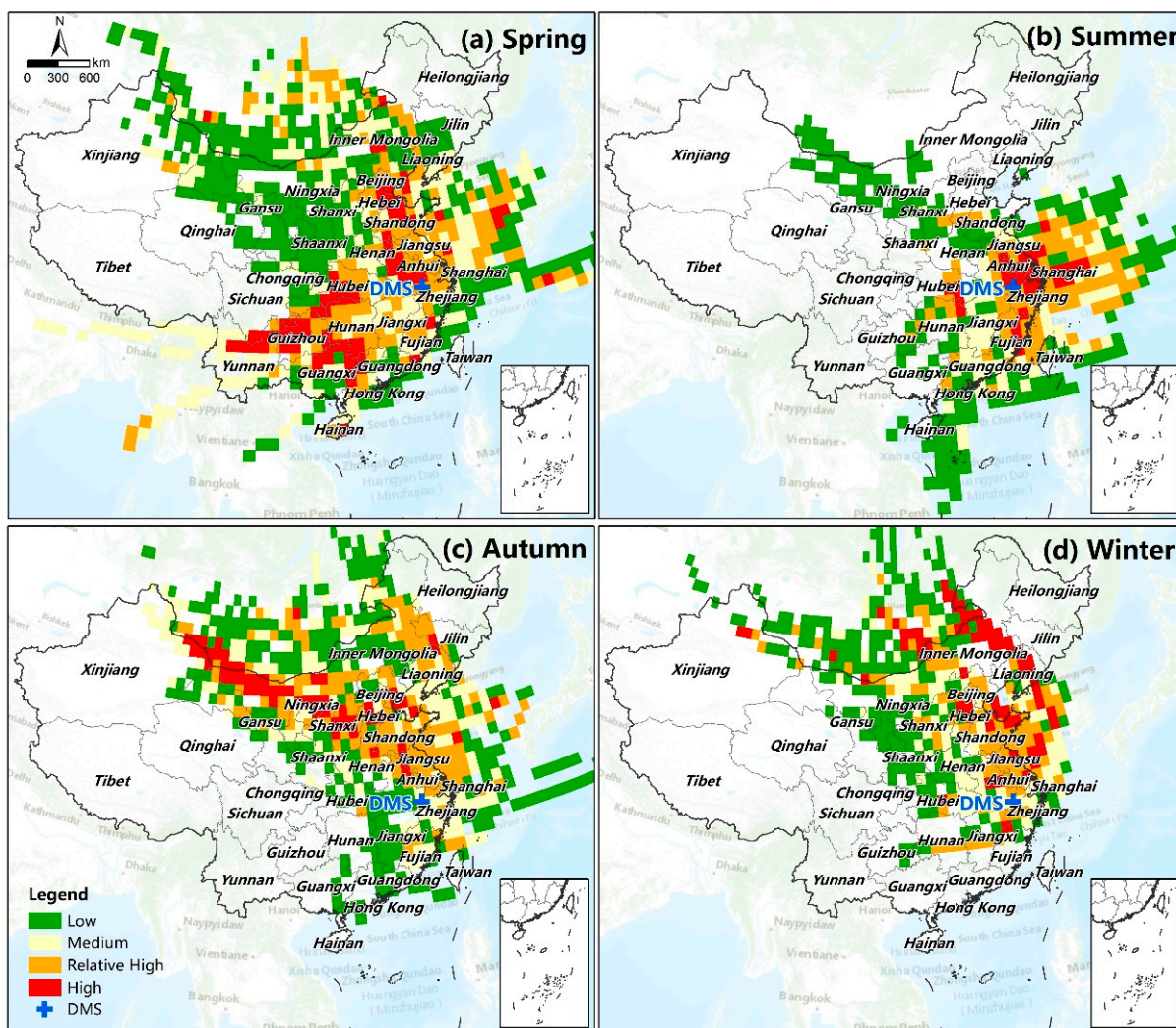


Figure 11. Geographical distributions of seasonal weighted potential sources of CO from 2020 to 2022 at DMS. The higher WPSCF represented the higher contribution from the areas to the CO concentration at DMS. The WPSCF were reclassified by Natural Break as low (<0.2), Medium (0.2–0.4), Relative-High (0.4–0.6), and High (>0.6) for better performance.

During the autumn and winter seasons, a significant proportion (29.1% and 29.3%) of air masses from the north skim the surface, moving through the heavily industrialized and populated zones of the Beijing-Tianjin-Hebei area, Shandong Province, and Jiangsu Province. This led to a marked surge in CO levels, with the northern air masses exhibiting

the highest CO concentrations. Specifically, the autumn northern air masses showed an enhancement of approximately 40 ppb. In comparison, their winter counterparts displayed a rise of around 9 ppb, compared to the respective seasonal averages (Figure 10 and Table 2). Except for the impacts of industrialization and urbanization, the heating period of North China, lasting from October to the following March, could play a crucial role in contributing to the seasonal increase of CO levels at DMS. Throughout the heating season, the widespread reliance on coal for heating led to extra CO emissions carried south by the winter monsoon, ultimately being recorded at our monitoring station. Further supporting this observation, data from the Atmospheric Infrared Sounder (AIRS) integrated on Aqua also revealed a high concentration of CO occurring from November to April in Northeast China, closely associated with the heating period [57]. Within 72 h, almost all air masses experienced a descent from high altitude to near ground level, then began to climb along the mountains around the last 20 h, when their trajectories mainly existed in the YRD region (Figures 9 and 10). This observation aligned with the high WPSCF values in Figure 11c,d, confirming that North China contributed significantly to the CO concentration.

Combined with the WPSCF analysis, it was worth noting the complex interplay of long-distance transportation and regional sources emissions within YRD shaped the CO concentration levels at the DMS site (Figure 11). The eastern Anhui, the western Jiangxi, Zhejiang, and Jiangsu provinces were the main potential source areas of CO at DMS, which was consistent with the previous studies [58]. The potential source areas identified in this study covered the major regions of the YRD, which provides further evidence that DMS could perfectly represent not only CO but also other greenhouse gases emitted homogeneously in the YRD region. Additionally, the emissions from the remoting regions, such as North China and Southeast Asia (including parts of South China), could influence the CO levels at DMS via long-distance transportation. Hence, the CO level is influenced not only by emissions within the YRD but also by contributions from surrounding areas or even distant regions.

3.3. Regional Representation of CO at DMS

3.3.1. Well-Mixed Atmosphere Conditions

Predominant surface wind directions varied throughout the year at LAN and DMS. As shown in Figure 12a, the CO concentrations at LAN strongly depended on surface wind direction, with notable variations observed across different wind directions. Higher CO concentrations were observed when the winds came from the ENE-E-ESE-SE-SSE sectors. Conversely, lower concentrations were observed in the NNE and SW sectors, which had the largest wind frequencies [17]. This dependency on wind direction suggested that the CO transport from specific local sources associated with prevailing wind patterns influenced the observed CO concentration at LAN. According to Figure 12b, the average CO concentration distribution displayed a uniform pattern across 16 wind directions at DMS, except for a comparatively lower value observed in the WSW sector during summer. The winds from NNW, NNE, and N relatively prevailed in spring, summer, and winter, whereas those from S and SSW prevailed in autumn. The uniform CO concentration pattern across all wind directions indicated a narrow range of average values throughout the measured periods. Also, this suggested that compared to LAN, the atmosphere at DMS exhibited a well-mixed condition with a relatively consistent concentration across various wind sectors within the same season. Based on Figure 13, the CO concentrations at DMS did not exhibit a significant dependency on surface wind direction and wind speed, and no significant reliance was found between the concentrations and wind frequency at DMS. Indeed, those were the fundamental conditions for a well-regional representative observation, ensuring that the data collection accurately represented a larger region under consideration. Combined with

Figure 11, the potential source areas extensively covered the most YRD areas. Hence, the wind-rose maps consistently supported that the CO observed at DMS could represent the atmospheric CO concentrations within the YRD well.

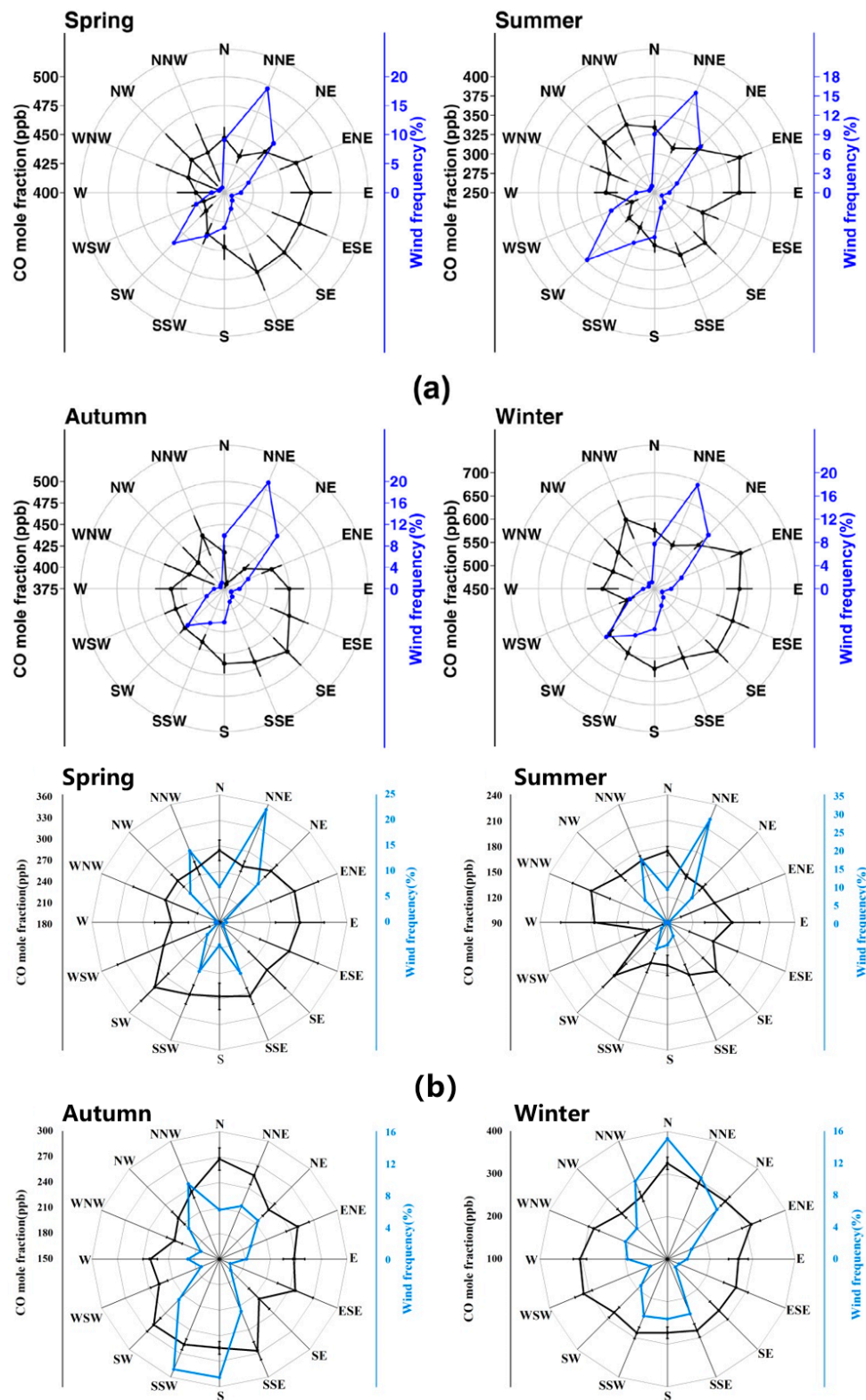


Figure 12. Comparison of wind-rose maps between (a) LAN and (b) DMS. The average CO concentrations were divided into 16 horizontal wind directions. Error bars in each direction indicate 95% confidence intervals. The maps of LAN were adapted from Liu’s work [17].

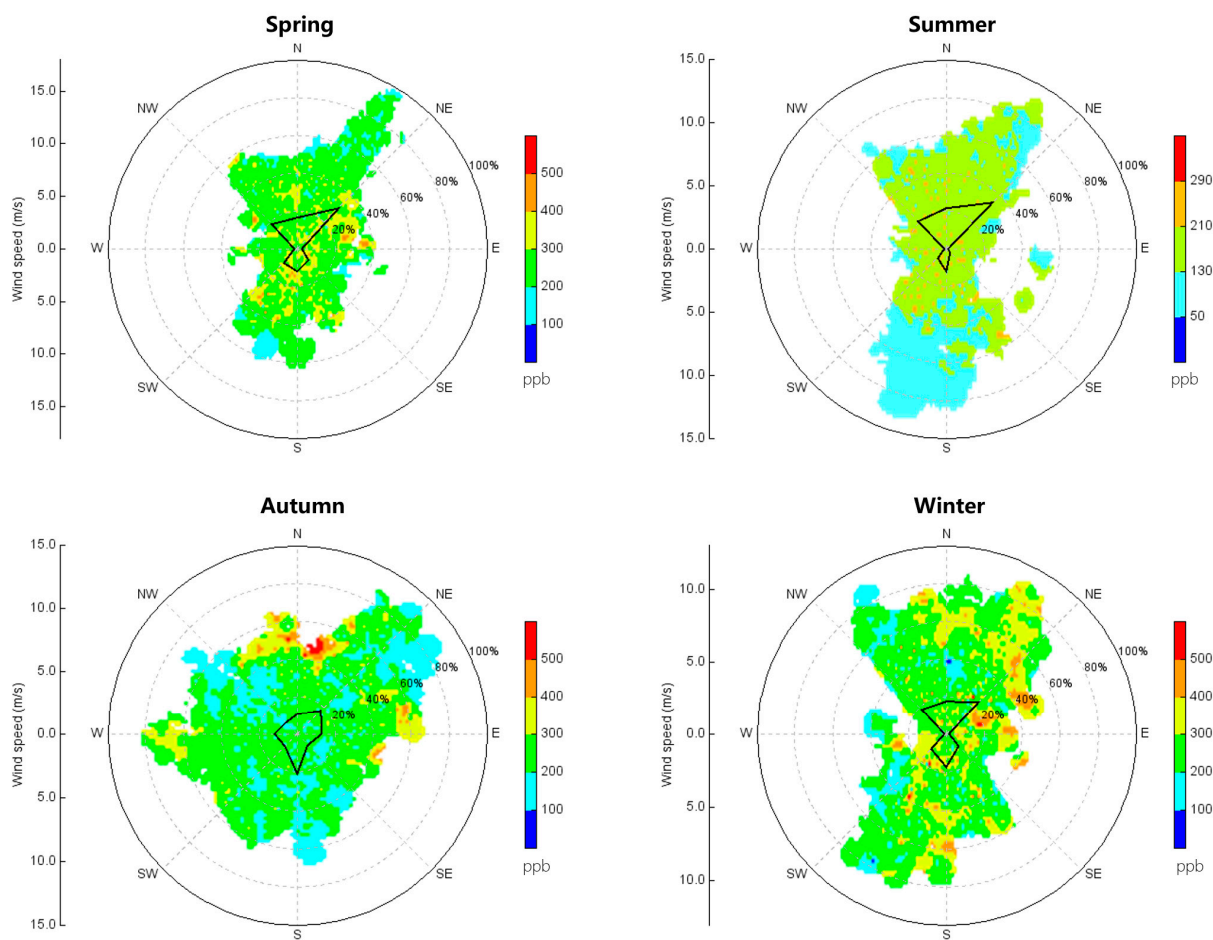


Figure 13. Non-parametric regression between wind direction, wind speed, and CO concentration at DMS. The percentage represented the wind frequency of the different wind directions.

3.3.2. Potential Influences of Human Activities

CO emissions are highly associated with human activities [59]. The amount of impervious surface area and the extension of nighttime light are important indicators in monitoring human activity intensity [47,60]. The adjacent land cover around DMS and LAN was compared to evaluate the potential influences of human activities. Based on CLCD in 2021, the surrounding land use and land cover for both DMS and LAN was mapped with a radius of 20 km in Figure 14a,b. The forest registered over 95% of land covers around DMS, and only 4.06% and 0.50% of the land were regarded as cropland and impervious surfaces, whereas LAN has a lower forest fraction (72.0%) and much higher fractions for cropland (20.71%) and impervious surfaces (6.0%). Compared with the other regional stations in China, the surrounding land cover of DMS occupied the highest forest fraction and low fractions of impervious surfaces and cropland (Table 3). Impervious surfaces are artificial hard surfaces that significantly impede water from infiltrating the ground, including building roofs, highways, roads, pavements, etc. Cropland was regarded as a semi-natural ecosystem with intensive agricultural management. Those two types of land use could reflect the intensity of anthropogenic activities surrounding monitoring sites. The scarcity of cropland and impervious surfaces surrounding DMS was a compelling indicator of reduced human activity compared to LAN. This inference aligns with the results of NTL data in Figure 14c,d, that DMS had a significantly lower NTL intensity than LAN, substantiating a lower degree of human-induced impacts within the surrounding region of DMS.

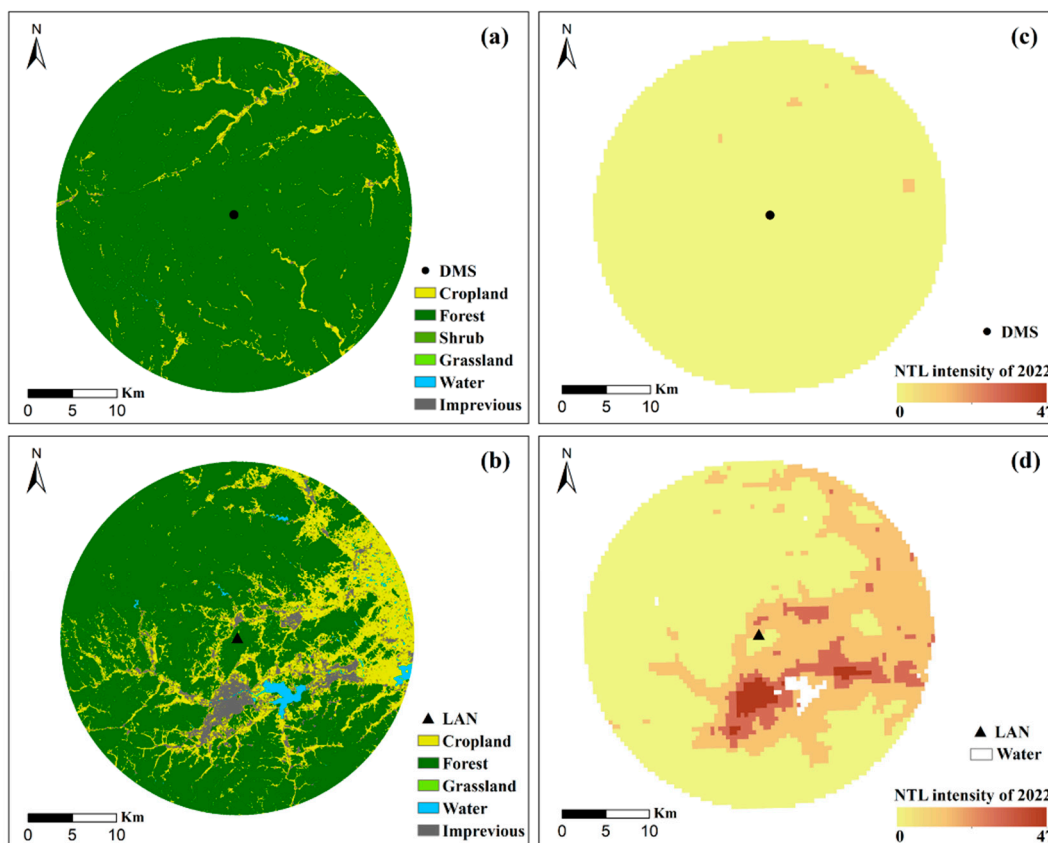


Figure 14. Annual CLCD in 2021 within a 20 km radius of DMS (a) and LAN (b) and NTL data in 2022 within a 20 km radius of DMS (c) and LAN (d).

Table 3. Proportion of different land cover in 2021 at DMS, LAN, LFS, SDZ, and WLG within a 20 km buffer.

	Class						
	Cropland	Forest	Shrub	Grassland	Water	Impervious	Barren
DMS	4.06	95.33	0.01	0.02	0.03	0.50%	-
LAN	20.71	71.84	-	-	1.19	6.00%	-
LFS	46.27	49.98	-	0.02	1.73	-	-
SDZ	15.28	73.19	0.06	3.98	3.65	-	-
WLG	5.54	0.02	0.09	74.27	0.39	-	19.70

3.3.3. Well Alliance with CAMS Reanalysis Data

The well-represented percentage for 14 buffers over the study period can determine what scope could be represented by the CO concentration detected at DMS (Table 4). The higher well-represented percentage referred to better representing the CO observations at DMS for the corresponding buffer.

According to Table 4 and Figure 15, the well-represented percentage increased first and then decreased with buffer radius increments. The highest well-represented percentage was around 82.8%, with buffer radiuses ranging from 3.75° to 5.25°, so the YRD could be well involved within these buffers. With a buffer radius smaller than 3.75°, the CO averages of CAMS were much higher than that of DMS, while with a buffer radius larger than 5.25°, although the CO averages of CAMS better fitted the DMS results, the well-represented percentage decreased significantly. To encapsulate, the CO observation at DMS could well represent the atmospheric CO mixing state of the YRD.

Table 4. CO concentrations and well-represented percentages for different buffers.

Stations	Buffer Radius (°)	Well-Represented Percentage (%)	CO Averages (ppb)	
DMS	In situ	-	233.4 ± 3.8	
	0.75	78.2	261.3 ± 4.0	
	1.50	79.4	256.3 ± 3.7	
	2.25	81.1	251.8 ± 3.4	
	3.00	82.3	246.5 ± 3.2	
	3.75	82.7	240.5 ± 2.9	
	4.50	82.8	236.5 ± 2.7	
	5.25	82.7	234.2 ± 2.6	
	CAMS	6.00	82.2	233.2 ± 2.4
		6.75	82.0	234.1 ± 2.3
		7.50	81.8	235.3 ± 2.2
		8.25	81.1	237.4 ± 2.1
9.00		80.3	237.2 ± 2.1	
9.75		79.5	235.2 ± 2.0	
	10.50	78.8	233.6 ± 2.0	
	11.25	78.4	232.5 ± 2.0	

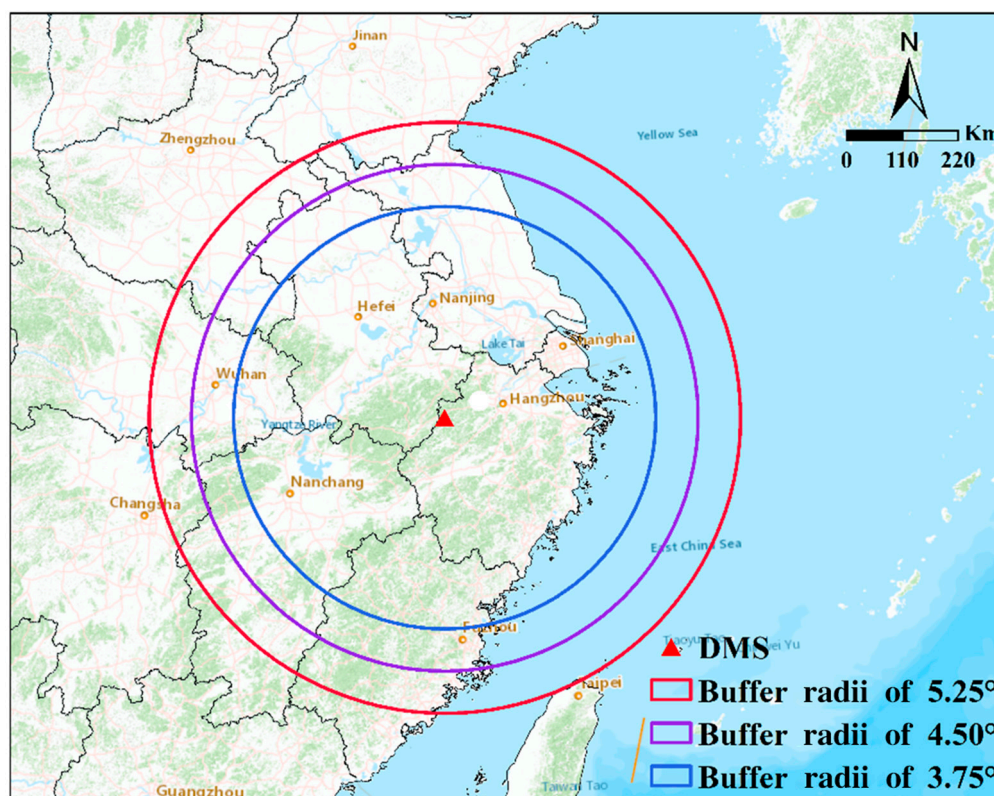


Figure 15. Centered on DMS, the buffer range with radii of 3.75°, 4.50°, and 5.25°.

Previous literature has found that the North China Plain, the Middle-lower Yangtze Plain, and the eastern region of LAN transported high CO to LAN, and large-scale strong source regions were evenly distributed around the station from 2011 to 2017 [17], which was similar to the situation at DMS to some extent (see Section 3.2).

According to the results, DMS had less impact on anthropogenic activities surrounding the station, and the atmospheric CO could be well mixed around DMS with well representing the regional CO levels of YRD.

4. Conclusions

The atmospheric CO concentration at a high-altitude station (DMS) in the YRD region, spanning from September 2020 to January 2022, was analyzed in this study to trace its

spatiotemporal characteristics and representativeness. At the seasonal scale, the additional energy consumption in cold seasons contributed to the elevated CO levels at the site, but the highest concentration peaked in March due to the combined effect of regional emissions within the YRD and air masses transported from Southeast Asia and North China. The diurnal cycle had a nocturnal peak and a morning valley but with a distinct afternoon climb, which was associated with the transport and discharge from the metropolitan cities in the YRD situated to the north and northeast of DMS. The cluster analysis and potential source analysis further confirmed that the air masses originating from North and Northeast China significantly influenced the CO records at DMS, and the air masses passing through the metropolis situated within the YRD accompanying high PSCF values contributed to a regional CO enhancement. The observation records at DMS aligned with the CO data provided by CAMS and well represented the CO levels of a radius ranging from 3.75° to 5.25° centered on DMS, within which areas the whole YRD could be enclosed. Additionally, DMS exhibited well-mixed air conditions and fewer local influences than LAN, a WMO/GAW regional background station. The CO concentrations observed at DMS could represent the regional CO levels of the YRD region well compared to the measurements currently deployed in the urban area in this region.

However, this study has certain limitations. The data span is relatively short, representing a preliminary analysis of CO monitoring at DMS. Future studies should incorporate multi-source data or additional atmospheric variables to analyze long-term data series. DMS will make significant contributions to air quality management and sustainable development in the YRD region in the future.

Author Contributions: Conceptualization, Y.L., Y.Y. and S.F.; methodology, S.L. (Shan Li), M.L. and B.C.; formal analysis, S.L. (Shuo Liu) and S.L. (Shan Li); writing—original draft preparation, Y.L. and S.L. (Shan Li); writing—review and editing, B.Q. and K.Z.; visualization, B.C. and Y.C.; supervision, S.F.; project administration, S.F.; funding acquisition, S.F. and B.Q. All authors have read and agreed to the published version of the manuscript.

Funding: This work was supported by the National Key Research and Development Program of China (2023YFC3705200), the National Natural Science Foundation of China (42275113), the Basic Public Welfare Funds of the Zhejiang Provincial of China (LGF22D050004), Zhejiang Provincial Natural Science Foundation of China (LTGS23D050001), and the Innovative Development Special Project of the China Meteorological Administration (CXFZ2022J046).

Institutional Review Board Statement: Not applicable.

Informed Consent Statement: Not applicable.

Data Availability Statement: The CO observation datasets presented in this article are not readily available because the data are part of an ongoing study. Requests to access the datasets should be directed to Prof. Shuangxi Fang (email: fangsx@zjut.edu.cn).

Acknowledgments: We thank the staff who have contributed to the system installation and maintenance at the Damingshan station in the past years.

Conflicts of Interest: The authors declare no conflicts of interest.

References

1. Thompson, A.M.; Cicerone, R.J. Atmospheric CH₄, CO and OH from 1860 to 1985. *Nature* **1986**, *321*, 148–150. [[CrossRef](#)]
2. Lashof, D.A.; Ahuja, D.R. Relative Contributions of Greenhouse Gas Emissions to Global Warming. *Nature* **1990**, *344*, 529–531. [[CrossRef](#)]
3. Thompson, A.M. The Oxidizing Capacity of the Earth's Atmosphere: Probable Past and Future Changes. *Science* **1992**, *256*, 1157–1165. [[CrossRef](#)]

4. Zheng, B.; Chevallier, F.; Yin, Y.; Ciais, P.; Fortems-Cheiney, A.; Deeter, M.N.; Parker, R.J.; Wang, Y.; Worden, H.M.; Zhao, Y. Global Atmospheric Carbon Monoxide Budget 2000–2017 Inferred from Multi-Species Atmospheric Inversions. *Earth Syst. Sci. Data* **2019**, *11*, 1411–1436. [[CrossRef](#)]
5. Duncan, B.N.; Strahan, S.E.; Yoshida, Y.; Steenrod, S.D.; Livesey, N. Model Study of the Cross-Tropopause Transport of Biomass Burning Pollution. *Atmos. Chem. Phys.* **2007**, *7*, 3713–3736. [[CrossRef](#)]
6. Silva, S.J.; Arellano, A.F. Characterizing Regional-Scale Combustion Using Satellite Retrievals of CO, NO₂ and CO₂. *Remote Sens.* **2017**, *9*, 744. [[CrossRef](#)]
7. Chen, Y.; Ma, Q.; Lin, W.; Xu, X.; Yao, J.; Gao, W. Measurement Report: Long-Term Variations in Carbon Monoxide at a Background Station in China’s Yangtze River Delta Region. *Atmos. Chem. Phys.* **2020**, *20*, 15969–15982. [[CrossRef](#)]
8. Klemm, O.; Hahn, M.K.; Giehl, H. Airborne, Continuous Measurement of Carbon Monoxide in the Lower Troposphere. *Environ. Sci. Technol.* **1996**, *30*, 115–120. [[CrossRef](#)]
9. Luo, H.; Tang, X.; Wu, H.; Kong, L.; Wu, Q.; Cao, K.; Song, Y.; Luo, X.; Wang, Y.; Zhu, J.; et al. The Impact of the Numbers of Monitoring Stations on the National and Regional Air Quality Assessment in China During 2013–2018. *Adv. Atmos. Sci.* **2022**, *39*, 1709–1720. [[CrossRef](#)] [[PubMed](#)]
10. Balzani Lööv, J.M.; Henne, S.; Legreid, G.; Staehelin, J.; Reimann, S.; Prévôt, A.S.H.; Steinbacher, M.; Vollmer, M.K. Estimation of Background Concentrations of Trace Gases at the Swiss Alpine Site Jungfraujoch (3580 m Asl). *J. Geophys. Res. Atmos.* **2008**, *113*, D22305. [[CrossRef](#)]
11. Kaiser, A.; Scheifinger, H.; Spangl, W.; Weiss, A.; Gilge, S.; Fricke, W.; Ries, L.; Cemas, D.; Jesenovec, B. Transport of Nitrogen Oxides, Carbon Monoxide and Ozone to the Alpine Global Atmosphere Watch Stations Jungfraujoch (Switzerland), Zugspitze and Hohenpeissenberg (Germany), Sonnblick (Austria) and Mt. Kravac (Slovenia). *Atmos. Environ.* **2007**, *41*, 9273–9287. [[CrossRef](#)]
12. Zhang, F.; Zhou, L.X.; Novelli, P.C.; Worthy, D.E.J.; Zellweger, C.; Klausen, J.; Ernst, M.; Steinbacher, M.; Cai, Y.X.; Xu, L.; et al. Evaluation of in Situ Measurements of Atmospheric Carbon Monoxide at Mount Waliguan, China. *Atmos. Chem. Phys.* **2011**, *11*, 5195–5206. [[CrossRef](#)]
13. Adame, J.A.; Cupeiro, M.; Yela, M.; Cuevas, E.; Carbajal, G. Ozone and Carbon Monoxide at the Ushuaia GAW-WMO Global Station. *Atmos. Res.* **2019**, *217*, 1–9. [[CrossRef](#)]
14. Fang, S.X.; Zhou, L.X.; Tans, P.P.; Ciais, P.; Steinbacher, M.; Xu, L.; Luan, T. In Situ Measurement of Atmospheric CO₂ at the Four WMO/GAW Stations in China. *Atmos. Chem. Phys.* **2014**, *14*, 2541–2554. [[CrossRef](#)]
15. Fang, S.; Tans, P.P.; Steinbacher, M.; Zhou, L.; Luan, T.; Li, Z. Observation of Atmospheric CO₂ and CO at Shangri-La Station: Results from the Only Regional Station Located at Southwestern China. *Tellus B Chem. Phys. Meteorol.* **2016**, *68*, 28506. [[CrossRef](#)]
16. Xiong, H.; Lin, Y.; Liu, S.; Zang, K.; Chen, Y.; Liu, P.; Liang, M.; Jiang, K.; Qing, X.; Qiu, S.; et al. Variations of Atmospheric CO Concentration from 2004 to 2019 at the Mt. Waliguan Station in China. *Atmos. Res.* **2022**, *271*, 106060. [[CrossRef](#)]
17. Liu, S.; Fang, S.; Liang, M.; Sun, W.; Feng, Z. Temporal Patterns and Source Regions of Atmospheric Carbon Monoxide at Two Background Stations in China. *Atmos. Res.* **2019**, *220*, 169–180. [[CrossRef](#)]
18. Wang, K.; Jiang, H. Analysis on the Spatio-Temporal Gradients of Carbon Monoxide in China by SCIAMACHY Remotely Sensed Data. In Proceedings of the MIPPR 2009: Remote Sensing and GIS Data Processing and Other Applications; SPIE: Bellingham, WA, USA, 2009; Volume 7498, pp. 765–772.
19. Huang, X.; Wang, T.; Talbot, R.; Xie, M.; Mao, H.; Li, S.; Zhuang, B.; Yang, X.; Fu, C.; Zhu, J.; et al. Temporal Characteristics of Atmospheric CO₂ in Urban Nanjing, China. *Atmos. Res.* **2015**, *153*, 437–450. [[CrossRef](#)]
20. Chen, C.; Liu, C.; Chen, R.; Wang, W.; Li, W.; Kan, H.; Fu, C. Ambient Air Pollution and Daily Hospital Admissions for Mental Disorders in Shanghai, China. *Sci. Total Environ.* **2018**, *613–614*, 324–330. [[CrossRef](#)] [[PubMed](#)]
21. Martin, F.; Fileni, L.; Palomino, I.; Vivanco, M.G.; Garrido, J.L. Analysis of the Spatial Representativeness of Rural Background Monitoring Stations in Spain. *Atmos. Pollut. Res.* **2014**, *5*, 779–788. [[CrossRef](#)]
22. Vitali, L.; Morabito, A.; Adani, M.; Assennato, G.; Ciancarella, L.; Cremona, G.; Giua, R.; Pastore, T.; Piersanti, A.; Righini, G.; et al. A Lagrangian Modelling Approach to Assess the Representativeness Area of an Industrial Air Quality Monitoring Station. *Atmos. Pollut. Res.* **2016**, *7*, 990–1003. [[CrossRef](#)]
23. Liu, S.; Su, H.; Tian, J.; Wang, W. An Analysis of Spatial Representativeness of Air Temperature Monitoring Stations. *Theor. Appl. Climatol.* **2018**, *132*, 857–865. [[CrossRef](#)]
24. The People’s Government of Lin’an District. *Lin’an Yearbook 2021*; The People’s Government of Lin’an District: Hangzhou, China, 2021.
25. Fang, S.-X.; Zhou, L.-X.; Masarie, K.A.; Xu, L.; Rella, C.W. Study of Atmospheric CH₄ Mole Fractions at Three WMO/GAW Stations in China. *J. Geophys. Res. Atmos.* **2013**, *118*, 4874–4886. [[CrossRef](#)]
26. Zellweger, C.; Steinbacher, M.; Buchmann, B. Evaluation of New Laser Spectrometer Techniques for In-Situ Carbon Monoxide Measurements. *Atmos. Meas. Tech.* **2012**, *5*, 2555–2567. [[CrossRef](#)]
27. Polissar, A.V.; Hopke, P.K.; Paatero, P.; Kaufmann, Y.J.; Hall, D.K.; Bodhaine, B.A.; Dutton, E.G.; Harris, J.M. The Aerosol at Barrow, Alaska: Long-Term Trends and Source Locations. *Atmos. Environ.* **1999**, *33*, 2441–2458. [[CrossRef](#)]

28. Wang, Y.Q.; Zhang, X.Y.; Draxler, R.R. TrajStat: GIS-Based Software That Uses Various Trajectory Statistical Analysis Methods to Identify Potential Sources from Long-Term Air Pollution Measurement Data. *Environ. Model. Softw.* **2009**, *24*, 938–939. [[CrossRef](#)]
29. Inness, A.; Ades, M.; Agustí-Panareda, A.; Barré, J.; Benedictow, A.; Blechschmidt, A.-M.; Dominguez, J.J.; Engelen, R.; Eskes, H.; Flemming, J.; et al. The CAMS Reanalysis of Atmospheric Composition. *Atmos. Chem. Phys.* **2019**, *19*, 3515–3556. [[CrossRef](#)]
30. Wagner, A.; Bennouna, Y.; Blechschmidt, A.-M.; Brasseur, G.; Chabrilat, S.; Christophe, Y.; Errera, Q.; Eskes, H.; Flemming, J.; Hansen, K.M.; et al. Comprehensive Evaluation of the Copernicus Atmosphere Monitoring Service (CAMS) Reanalysis against Independent Observations: Reactive Gases. *Elem. Sci. Anthr.* **2021**, *9*, 00171. [[CrossRef](#)]
31. Flemming, J.; Benedetti, A.; Inness, A.; Engelen, R.J.; Jones, L.; Huijnen, V.; Remy, S.; Parrington, M.; Suttie, M.; Bozzo, A.; et al. The CAMS Interim Reanalysis of Carbon Monoxide, Ozone and Aerosol for 2003–2015. *Atmos. Chem. Phys.* **2017**, *17*, 1945–1983. [[CrossRef](#)]
32. Langerock, B.; Arola, A.; Basart, S.; Benedictow, A.; Bennouna, Y.; Blechschmidt, A.-M.; Bouarar, I.; Cuevas, E.; Errera, Q.; Eskes, H.J.; et al. *Validation Report of the CAMS Near-Real-Time Global Atmospheric Composition Service Period March–May 2022*; European Commission: Bruxelles, Belgium, 2022. [[CrossRef](#)]
33. Schoenhardt, A.; Arola, A.; Benedictow, A.; Bennouna, Y.; Bouarar, I.; Cuevas, E.; Errera, Q.; Eskes, H.J.; Griesfeller, J.; Basart, S.; et al. *Validation Report of the CAMS Near-Real-Time Global Atmospheric Composition Service Period September–November 2022*; European Commission: Bruxelles, Belgium, 2023.
34. Yang, J.; Huang, X. The 30 m Annual Land Cover Dataset and Its Dynamics in China from 1990 to 2019. *Earth Syst. Sci. Data* **2021**, *13*, 3907–3925. [[CrossRef](#)]
35. Chen, Z.; Yu, B.; Yang, C.; Zhou, Y.; Yao, S.; Qian, X.; Wang, C.; Wu, B.; Wu, J. An Extended Time Series (2000–2018) of Global NPP-VIIRS-like Nighttime Light Data from a Cross-Sensor Calibration. *Earth Syst. Sci. Data* **2021**, *13*, 889–906. [[CrossRef](#)]
36. Ma, T.; Zhou, C.; Pei, T.; Haynie, S.; Fan, J. Quantitative Estimation of Urbanization Dynamics Using Time Series of DMSP/OLS Nighttime Light Data: A Comparative Case Study from China's Cities. *Remote Sens. Environ.* **2012**, *124*, 99–107. [[CrossRef](#)]
37. Zhou, Y.; Smith, S.J.; Zhao, K.; Imhoff, M.; Thomson, A.; Bond-Lamberty, B.; Asrar, G.R.; Zhang, X.; He, C.; Elvidge, C.D. A Global Map of Urban Extent from Nightlights. *Environ. Res. Lett.* **2015**, *10*, 054011. [[CrossRef](#)]
38. Sutton, P.; Roberts, D.; Elvidge, C.; Baugh, K. Census from Heaven: An Estimate of the Global Human Population Using Night-Time Satellite Imagery. *Int. J. Remote Sens.* **2001**, *22*, 3061–3076. [[CrossRef](#)]
39. WDCGG (World Data Centre for Greenhouse Gases). Available online: <https://gaw.kishou.go.jp/publications/summary> (accessed on 20 December 2024).
40. Qi, H.; Lin, W.; Xu, X.; Yu, X.; Ma, Q. Significant Downward Trend of SO₂ Observed from 2005 to 2010 at a Background Station in the Yangtze Delta Region, China. *Sci. China Chem.* **2012**, *55*, 1451–1458. [[CrossRef](#)]
41. Guo, H.; Wang, T.; Simpson, I.J.; Blake, D.R.; Yu, X.M.; Kwok, Y.H.; Li, Y.S. Source Contributions to Ambient VOCs and CO at a Rural Site in Eastern China. *Atmos. Environ.* **2004**, *38*, 4551–4560. [[CrossRef](#)]
42. Ou-Yang, C.-F.; Lin, N.-H.; Lin, C.-C.; Wang, S.-H.; Sheu, G.-R.; Lee, C.-T.; Schnell, R.C.; Lang, P.M.; Kawasato, T.; Wang, J.-L. Characteristics of Atmospheric Carbon Monoxide at a High-Mountain Background Station in East Asia. *Atmos. Environ.* **2014**, *89*, 613–622. [[CrossRef](#)]
43. Wang, H.; Yu, D.; Zang, K.; Hong, H.; Qiu, S.; Xiong, H.; Li, J.; Qin, X.; Jiang, K.; Fang, S. Characteristics of CO concentration and analysis of transport pathways at the Longfengshan background atmosphere station. *J. Environ. Sci.* **2022**, *42*, 392–400. [[CrossRef](#)]
44. Zhao, Z.; He, Q.; Lu, Z.; Zhao, Q.; Wang, J. Analysis of Atmospheric CO₂ and CO at Akedala Atmospheric Background Observation Station, a Regional Station in Northwestern China. *Int. J. Environ. Res. Public Health* **2022**, *19*, 6948. [[CrossRef](#)] [[PubMed](#)]
45. Choi, Y.; Kanaya, Y.; Park, S.-M.; Matsuki, A.; Sadanaga, Y.; Kim, S.-W.; Uno, I.; Pan, X.; Lee, M.; Kim, H.; et al. Regional Variability in Black Carbon and Carbon Monoxide Ratio from Long-Term Observations over East Asia: Assessment of Representativeness for Black Carbon (BC) and Carbon Monoxide (CO) Emission Inventories. *Atmos. Chem. Phys.* **2020**, *20*, 83–98. [[CrossRef](#)]
46. Gao, L.; Zhang, M.; Han, Z. Model Analysis of Seasonal Variations in Tropospheric Ozone and Carbon Monoxide over East Asia. *Adv. Atmos. Sci.* **2009**, *26*, 312–318. [[CrossRef](#)]
47. Zhang, X.; Liu, J.; Han, H.; Zhang, Y.; Jiang, Z.; Wang, H.; Meng, L.; Li, Y.C.; Liu, Y. Satellite-Observed Variations and Trends in Carbon Monoxide over Asia and Their Sensitivities to Biomass Burning. *Remote Sens.* **2020**, *12*, 830. [[CrossRef](#)]
48. Sikder, H.A.; Suthawaree, J.; Kato, S.; Kajii, Y. Surface Ozone and Carbon Monoxide Levels Observed at Oki, Japan: Regional Air Pollution Trends in East Asia. *J. Environ. Manag.* **2011**, *92*, 953–959. [[CrossRef](#)] [[PubMed](#)]
49. Suthawaree, J.; Kato, S.; Takami, A.; Kadana, H.; Toguchi, M.; Yogi, K.; Hatakeyama, S.; Kajii, Y. Observation of Ozone and Carbon Monoxide at Cape Hedo, Japan: Seasonal Variation and Influence of Long-Range Transport. *Atmos. Environ.* **2008**, *42*, 2971–2981. [[CrossRef](#)]
50. Li, Y.; Ma, Z.; Han, T.; Quan, W.; Wang, J.; Zhou, H.; He, D.; Dong, F. Long-Term Declining in Carbon Monoxide (CO) at a Rural Site of Beijing during 2006–2018 Implies the Improved Combustion Efficiency and Effective Emission Control. *J. Environ. Sci.* **2022**, *115*, 432–442. [[CrossRef](#)]

51. Ou-Yang, C.-F.; Hsieh, H.-C.; Wang, S.-H.; Lin, N.-H.; Lee, C.-T.; Sheu, G.-R.; Wang, J.-L. Influence of Asian Continental Outflow on the Regional Background Ozone Level in Northern South China Sea. *Atmos. Environ.* **2013**, *78*, 144–153. [[CrossRef](#)]
52. Chiang, C.-K.; Fan, J.-F.; Li, J.; Chang, J.S. Impact of Asian Continental Outflow on the Springtime Ozone Mixing Ratio in Northern Taiwan. *J. Geophys. Res. Atmos.* **2009**, *114*, D24304. [[CrossRef](#)]
53. Cheung, V.T.F.; Wang, T. Observational Study of Ozone Pollution at a Rural Site in the Yangtze Delta of China. *Atmos. Environ.* **2001**, *35*, 4947–4958. [[CrossRef](#)]
54. Pan, X.L.; Kanaya, Y.; Wang, Z.F.; Liu, Y.; Pochanart, P.; Akimoto, H.; Sun, Y.L.; Dong, H.B.; Li, J.; Irie, H.; et al. Correlation of Black Carbon Aerosol and Carbon Monoxide in the High-Altitude Environment of Mt. Huang in Eastern China. *Atmos. Chem. Phys.* **2011**, *11*, 9735–9747. [[CrossRef](#)]
55. Gao, J.; Wang, T.; Ding, A.; Liu, C. Observational Study of Ozone and Carbon Monoxide at the Summit of Mount Tai (1534 m a.s.l.) in Central-Eastern China. *Atmos. Environ.* **2005**, *39*, 4779–4791. [[CrossRef](#)]
56. Chen, Y.; Lu, Y.; Qi, B.; Ma, Q.; Zang, K.; Lin, Y.; Liu, S.; Pan, F.; Li, S.; Guo, P.; et al. Atmospheric CO₂ in the Megacity Hangzhou, China: Urban-Suburban Differences, Sources and Impact Factors. *Sci. Total Environ.* **2024**, *926*, 171635. [[CrossRef](#)] [[PubMed](#)]
57. Wang, J.; Zhan, Q.; Guo, H. The Morphology, Dynamics and Potential Hotspots of Land Surface Temperature at a Local Scale in Urban Areas. *Remote Sens.* **2016**, *8*, 18. [[CrossRef](#)]
58. Hu, C.; Liu, S.; Wang, Y.; Zhang, M.; Xiao, W.; Wang, W.; Xu, J. Anthropogenic CO₂ Emissions from a Megacity in the Yangtze River Delta of China. *Environ. Sci. Pollut. Res.* **2018**, *25*, 23157–23169. [[CrossRef](#)] [[PubMed](#)]
59. Khalil, M.a.K.; Rasmussen, R.A. Global Decrease in Atmospheric Carbon Monoxide Concentration. *Nature* **1994**, *370*, 639–641. [[CrossRef](#)]
60. Wu, C.; Murray, A.T. Estimating Impervious Surface Distribution by Spectral Mixture Analysis. *Remote Sens. Environ.* **2003**, *84*, 493–505. [[CrossRef](#)]

Disclaimer/Publisher’s Note: The statements, opinions and data contained in all publications are solely those of the individual author(s) and contributor(s) and not of MDPI and/or the editor(s). MDPI and/or the editor(s) disclaim responsibility for any injury to people or property resulting from any ideas, methods, instructions or products referred to in the content.